FIRST PRINCIPLES INVESTIGATION OF LATTICE DYNAMICAL PROPERTIES OF CU-BASED CHALCOPYRITE SEMICONDUCTORS AND HIGH DIELECTRIC CONSTANT MATERIALS

by

CİHAN PARLAK

THESIS SUBMITTED TO
THE GRADUATE SCHOOL OF NATURAL AND APPLIED SCIENCES
OF
THE ABANT İZZET BAYSAL UNIVERSITY
IN PARTIAL FULFILLMENT OF THE REQUIREMENTS FOR THE
DEGREE OF
DOCTOR OF PHILOSOPHY
IN
THE DEPARTMENT OF PHYSICS

MARCH 2008

Approval of the Graduate School of Natural Sciences

Prof. Dr. Nihat Çelebi

Director

I certify that this thesis satisfies all the requirements as a thesis for the degree of Doctor of Philosophy.

Prof. Dr. Ahmet Turan Alan

Head of Physics Department

This is to certify that we have read this thesis and that in our opinion it is fully adequate, in scope and quality as a thesis for the degree of Doctor of Philosophy.

Assoc. Prof. Dr. Resul Eryiğit

Supervisor

Examining Committee Members

1. Assoc. Prof. Dr. Resul Eryiğit .....
2. Prof. Dr. Yüksel Ergün .....
3. Assoc. Prof. Dr. Ahmet Varilci .....
4. Assoc. Prof. Dr. Cem Yüce .....
5. Assoc. Prof. Dr. Cabir Terzioğlu .....

ABSTRACT

FIRST PRINCIPLES INVESTIGATION OF LATTICE DYNAMICAL PROPERTIES OF CU-BASED CHALCOPYRITE SEMICONDUCTORS AND HIGH DIELECTRIC CONSTANT MATERIALS

Parlak, Cihan

Ph.D., Department of Physics

Supervisor: Assoc. Prof. Dr. Resul Eryiğit

March 2008, 100 pages

We have planned to study two subjects: First principle investigation of hydrostatic pressure dependence of structural, elastic and lattice dynamical properties of Cu-based ternary semiconductors and electronic, dielectric and lattice dynamical properties of some perovskite structures that have very large low frequency dielectric constants.

Firstly we have performed an *ab initio* study of volume dependence of elastic and lattice dynamical properties of chalcopyrite semiconductor $CuGaSe_2$ and $CuAlS_2$. The calculations have been carried out within the local density functional approximation using norm-conserving pseudopotentials and a plane-wave basis. Born effective charge tensors, dielectric permitivity tensors, the phonon frequencies at the Brillouin zone center and their Grüneisen parameters are calculated using density functional perturbation theory. We compare the Grüneisen

parameters of the calculated quantities with those of zinc-blende type materials and found similar trends. Calculated elastic stiffness constants show pseudocubic behavior.

As a second research topic, we report the results of an *ab initio* study of electronic, dielectric and lattice dynamical properties of high dielectric constant perovskite-derived oxide $Na_{1/2}Bi_{1/2}Cu_3Ti_4O_{12}$. The calculations have been carried out within the local spin density functional approximation using norm-conserving pseudopotentials and a plane-wave basis. The ground state is found to be antiferromagnetic direct-band gap semiconductor. Lattice dynamical properties, such as Born effective charge tensors, dielectric permittivity tensors, and phonon frequencies at the Brillouin zone center were calculated using density functional perturbation theory and found to be similar to more studied $CaCu_3Ti_4O_{12}$ and $CdCu_3Ti_4O_{12}$ compounds. The calculated electronic ($\epsilon_\infty \approx 11.5$) and static ($\epsilon_0 \approx 150$) dielectric constants indicate that the observed high dielectric constant is extrinsic in origin. The main contribution to the static dielectric constant is found to be due to a low frequency (50 cm^{-1}) infrared-active mode which has a large mode effective charge.

Keywords: Chalcopyrite semiconductors, high dielectric constant materials, Born effective charges, phonon frequencies, dielectric permitivity tensors.

ÖZET

TEMEL İLKELERLE BAKIR TABANLI KALKOPİRİT YARIİLETKENLER VE YÜKSEK DİELEKTRİK SABİTLİ MALZEMELERİN ÖRGÜ DİMAMİĞİ ÖZELLİKLERİNİN İNCELENMESİ

Parlak, Cihan

Doktora, Fizik Bölümü

Tez Danışmanı: Doç. Dr. Resul Eryiğit

Mart 2008, 100 sayfa

Bakır tabanlı üçlü yarıiletkenlerin yapısal, elastik ve örgü dinamiği özelliklerinin basınca bağımlılığı ve çok yüksek genişlikte düşük frekans dielektrik sabitli bazı perovskite yapıların elektronik, yapısal ve dielektrik özelliklerinin temel ilkelerden incelenmesi olarak iki konu çalışmayı planlamıştık.

Öncelikle kalkopirit yarı iletkenler $CuGaSe_2$ and $CuAlS_2$'nin hacime bağlı elastik ve örgü dinamiği özellikleri üzerine *ab initio* hesaplamalar yaptık. Hesaplamalar yerel yoğunluk yaklaşımı çerçevesinde norm korunumlu sanal potansiyeller ve düzlem dalga tabanı kullanılarak gerçekleştirilmiştir. Born etkin yük tensörleri, dielektrik geçirgenlik tensörleri, Brillouin bölge merkezli fonon frekansları ile bunların grüneissen parametreleri, yoğunluk fonksiyonel tedirginme teorisi kullanılarak hesaplandı. Hesaplanan büyüklüklerin grüneissen parametreleri çinko-blende türü yapıların ki ile aynı biçimde olduğu bulundu. Ayrıca hesaplanan elastik-sertlik katsayılarının sanal kübik davranış gösterdiği tespit edildi.

İkinci araştırma konusu olarak, yüksek dielektrik sabitli perovskite türevi oksit $Na_{1/2}Bi_{1/2}Cu_3Ti_4O_{12}$ malzemesinin elektronik, dielektrik ve örgü dinamiği özelliklerinin *ab initio* sonuçlarını rapor ettik. Hesaplamalar yerel spin yoğunluk yaklaşımı, norm korunumlu sanal potansiyeller ve düzlem dalga tabanı kullanılarak yapıldı. Taban durumu direk bant aralıklı antiferromanyetik yarıiletken olarak bulundu. Born etkin yük tensörleri, dielektrik geçirgenlik tensörleri ve Brillouin bölge merkezli fonon frekansları gibi örgü dinamiği özellikleri yerel yoğunluk tedirginme teorisi ile hesaplanarak, daha önce sıklıkla çalışılan $CaCu_3Ti_4O_{12}$ ve $CdCu_3Ti_4O_{12}$ malzemelerine benzerlik gösterdiği tespit edildi. Hesaplanan elektronik ($\epsilon_\infty \approx 11.5$) ve statik ($\epsilon_0 \approx 150$) dielektrik katsayıları, gözlenen yüksek dielektrik katsayılarının dışsal nedenli olduğunu göstermiştir. Statik dielektrik sabitine temel katkı düşük frekanslı (50 cm^{-1}) yüksek mod etkin yüke sahip kızıl ötesi aktif moddan geldiği bulundu.

Anahtar Kelimeler: Kalkopirit yarıiletkenler, yüksek dielektrik sabitli malzemeler, Born ektin yük tensörleri, fonon frekansları, dilelektrik geçirgenlik tensörleri.

To My Family ...

ACKNOWLEDGEMENTS

I would like to thank my advisor, Dr. Resul Eryiğit for his support, guidance, patience and encouragement during years of my work as a graduate student at AIBU. I am obliged for his continuous guidance and support and thank to him for his help in the revision of scientific content and style of this dissertation. And I want to thank him not only for guidance for scientific content but also his guidance for all contents of life.

I am thankful to my family, for their support, patience, understanding...

This work was supported by Tübitak under grant no. TBAG-2449(104T057) and AIBU Research Fund grant no. 04.03.02.199.

TABLE OF CONTENTS

LIST OF TABLES

LIST OF FIGURES

CHAPTER 1

INTRODUCTION

Today's technology needs to investigate of properties of the number of materials both theoretically and experimentally, especially for energy and computer sectors. And condensed matter physics can help to design the materials needed, theoretically with the help of the recent theoretical studies and as well as the development in computer technology. The aim of these thesis investigate theoretically, important properties of two type of materials both so crucial for technological devices especially as mentioned before solar materials for photovoltaic device applications and capacitative elements for computers, namely chalcopyrite semiconductors $CuGaSe_2$ and $CuAlS_2$ and high dielectric constant material $Na_{1/2}Bi_{1/2}Cu_3Ti_4O_{12}$ (NBCTO) respectively.

Experimental works on mentioned materials still continue with increasing speed. In this manner the theoretical understanding of properties of these materials is becoming very important for future developments and increasing efficiency of uses of these materials for device technology. And a useful tool of theoretical condensed matter physics to deal with the electronic and lattice properties of solids is density functional theory (DFT) developed by Hohenberg-Kohn [1] and Kohn-Sham [2]. This theory, which was established in 1960s, has been immensely popular for accuracy and predictive power and the additional advantage of density functional theory can be using complex materials such as proteins (as DNA) and carbon nanotubes.

Density functional theory, in its many forms helped in understanding many different properties of systems. In condensed matter applications, it is generally

used within so called local density approximation (LDA) and pseudopotentials to account for the interaction between the valance electrons and the nuclei. In Section 2, we will review the basics of this theory and its implementation with a plane-wave basis.

The study of characteristic phonon frequencies is one of the most important methods for the characterization of strained materials. And the number of properties depend on their vibrational properties especially infrared, Raman and neutron-diffractions, the thermal properties such as thermal expansion coefficient, heat capacity and thermodynamical Grüneisen parameters. The first principle investigations of phonon frequencies can be investigate in density functional perturbation theory(DFPT) [3], frozen phonon [4] or direct method approach with respective advantage and disadvantages. Partly because of its computational ease, the so called frozen-phonon method [4] was the first *ab initio* phonon method. This method tried to find the phonon displacement pattern and calculate the energy difference between the perfect crystal and the crystal where the atoms are displaced according to particular phonon pattern. This technique is good for phonons at high symmetry points of the Brillouin zone. For a phonon at an arbitrary point in Brillouin zone, the displacement pattern would require a large unit cell and calculation becomes prohibitively large. A different approach to *ab initio* phonon problem is so called linear response approach [3]. In this approach, one considers phonon as a perturbation an the electronic density of the crystal and phonon frequencies are computed from the linear response of the crystal. This method has the added advantage that one can consider other perturbations, such as electrical field, which is important for the longitudinal optical modes of polar materials.

Lattice dynamical properties, such as effective charges, phonon frequencies

and low frequency dielectric constants provide crucial information about the structure of the material and pressure dependence of these properties important tool for investigations. Shifted phonon frequencies are signatures of strain state of the material and can be used to clarify mode structure by Raman scattering. Elastic properties of the material are another important ingredient of such an investigation. In this study we have investigate pressure dependence of lattice dynamical and elastic properties of chalcopyrite semiconductors $CuGaSe_2$ and $CuAlS_2$ and lattice dynamical and electronical properties of high dielectric material NBCTO.

First part of this dissertation is to use a first principles linear response approach to delineate the lattice dynamical properties, such as Brillouin zone center phonon frequencies, Born effective charge and dielectric permittivity tensors and elastic compliance tensor of chalcopyrite $CuAlS_2$ and $CuGaSe_2$ under hydrostatic pressure. Pressure is used as an important perturbational probe of the electronic, optical and lattice dynamical properties of materials[5]. Chalcopyrite lattice structure is a deformed super-structure of zinc-blende type structure and the phonon modes at the Brillouin zone center can be mapped to zone center and several zone boundary modes of zinc-blende structure[6, 7, 8]. Pressure dependence of lattice dynamical properties of zinc-blende compounds show certain trends, such as a negative mode Grüneisen parameter for transverse acoustic modes, especially towards Brillouin zone boundaries and decrease of effective charges under pressure[9]. In this study, we try to delineate the extent of the relationship between the pressure-dependence of lattice dynamical properties of zinc-blende and related ternary compounds.

There has been a number of suggestion, for the mechanism of colossal dielectric behavior. The second research topic of these study, as part of clarifying possi-

ble mechanisms of large dielectric constant, we have chosen $Na_{1/2}Bi_{1/2}Cu_3Ti_4O_{12}$ (NBCTO) as a test material and will report the results of *ab initio* density functional calculations to investigate the lattice dynamical and dielectric properties of NBCTO, to understanding of mechanism and properties of high dielectrics. High dielectric constant materials (with dielectric constant grater than $\varepsilon_0 > 7$), are important for technological applications such as wireless communication systems, for design of big memory for computers, namely as capacitors, resonators or filters and this allow minimization of electronic devices which are in increasing demand. And generally technology needs the finding new high dielectric constant materials instead of silicon based materials. In last decade $CaCu_3Ti_4O_{12}$ (CCTO) was reported as a high dielectric constant material which ε_0 value practically independent of temperature and frequency, both so important for device technology. Generally capacitative devices need to have static dielectric constant values to operate properly under variety of conditions, if the static dielectric constant strongly varying in temperature , device not operate properly[10]. After reported CCTO, research going on in this topic with increasing speed and a few materials have reported as a high-k material. And all this materials have similar dielectric behavior, as the frequency dependence of the complex dielectric function shows a Debye-like relaxational behavior, and nearly independence of temperature and frequency. Subramanian *et al.* [11] discussed a lot of compounds with the CCTO structure in the $ACu_3M_4O_{12}$(A=alkali, alkaline-earth metal, rareearth metal or vacancy, M=transition metal) system. They reported that more than ten compounds have dielectric constants larger than 1000 at room temperature and one of these materials is NBCTO. In literature, limited experimental data available about NBCTO. This study will help to future studies related by similar properties of similar materials.

The plan of the thesis is as follows; in Section 2, we give a brief overview of the main theory of density functional theory in pseudopotential plane-wave implementation. Section 3 is about Cu-based chalcopyrite semiconductors, details of calculations, brief explanation of lattice structure and lattice dynamical results displayed and discussed. And about high dielectric constant materials, some previous experimental as well as theoretical work on lattice dynamical and electronic properties of these type of materials displayed and details of calculations, our calculated born effective charges, phonon frequencies and dielectric constants displayed and discussed in section 4. Thesis concludes with discussion and further research suggestion in Section 5.

CHAPTER 2

DENSITY FUNCTIONAL THEORY

A system as solid, can be described as the system by a number of electrons and nuclei interacting through coulombic (electrostatic) forces. The first observation is the timescale associated to motion of nuclei is much slower than that associated to electrons and the mass of nuclei much greater than electrons. From this observation, one can entangling the nuclear degrees of freedom is called "adiabatic approximation" (or Born-Oppenheimer approximation).

With this approximation, one transforms the problem into two parts; the problem of electrons as if the nuclei are stationary and problems of nuclei moving on a potential energy surface determined by the electronic distribution.

The solution of the first problem would give the electronic energy band structure and electronic wave functions of the crystal, while the solution to second problem are the vibrational properties of the crystal.

Let us start with the first problem, here we have N interacting electrons in an external potential, created by stationary nuclei. This system is described quantum mechanically by the solutions of Schrödinger many body equation;

$$H\psi(\vec{r}_1, ..., \vec{r}_N) = E\psi(\vec{r}_1, ..., \vec{r}_N) \tag{2.1}$$

where H in the Hamiltonian:

$$H = -\frac{1}{2m_e}\sum_{i=1}^{N}\nabla_i^2 - \sum_{i=1}^{N}V_{ext}(\vec{r}_i) + \frac{e^2}{2}\sum_{i\neq j}\frac{1}{|\vec{r}_i - \vec{r}_j|} \tag{2.2}$$

where $\vec{r_i}$ is the position of the i^{th} electron and $V_{ext}(\vec{r_i})$ is the external potential that act on the electron i. In these formulas we are using atomic units, where $\hbar = 1$; if $m_e = \frac{1}{2}$ and $e^2 = 2$ then the energies are in Rydberg (Ryd) or if $m_e = 1$, $e^2 = 1$, energies are in Hartree (Ha).

In practise, the solution of Equation (2.1) cannot be found analytically or numerically in full quantum-mechanical framework, because coulombic form couples all the electronic degrees of freedom. To overcome this problem, its convenient to find the ground-state charge density, which can also be used to calculate the observable ground-state properties of the crystal in stead of to find many-body wave-function which solve Equation (2.1).

Practically, Equation (2.2) is replaced by equation derived from density functional theory (DFT) of Hohenberg and Kohn [1]. This theory shows that the external potential acting on electrons is a functional of the ground-state charge density. This potential, in turn, determines the ground-state wave-function and therefore all the ground-state properties of the electronic system are uniquely determined by its ground-state charge density distribution.

An important ground-state observable is the total energy of the system. Charge density can be found as the function that minimizes the total energy functional as demonstrated by Kohn and Sham (KS) [2].

Formally, one can write the ground-state energy of the many-body system as the expectation value of the Hamiltonian as;

$$G[n] =< \psi_0|H|\psi_0 > \tag{2.3}$$

Let us specialize the situation to properties of periodic solids, where nuclear position are fixed by the introduction of Bravais lattice vectors K_μ, and by the choice of basis vectors τ_s which characterize the positions of the nuclei inside the

unit cell so that the total energy of the electrons and the nuclei can be written as;

$$E_{tot} = E_{i-i} + G[n] \tag{2.4}$$

where E_{i-i} , the coulombic potential energy of the ionic subsystem which can be computed as;

$$E_{i-i} = \frac{e^2}{2} \sum_{\mu\nu}{}' \sum_{ss_1} \frac{Z_s Z_{s_1}}{|R_\mu + \tau_s - R_\nu - \tau_{s_1}|} \tag{2.5}$$

where Z_s, the charge of nucleus at τ_s and prime on summation indicates that $\mu = \nu$ and $s = s_1$ term is omitted from the sum.

Kohn and Sham introduced a new functional $G[n]$ with help of wave-functions of independent electron gas with the same density as the interacting system.

Within this approach, let $|\psi_i>$ be the single particle wave functions of non-interacting system, then the kinetic energy would be

$$T = -\frac{1}{2m_e} \sum_i f_i < \psi_i|\nabla^2|\psi_i > \tag{2.6}$$

where f_i is the Fermi function, which is equal to 2 (taking into account spin degeneracy) if the energy of the i^{th} level is less than Fermi energy and equals 0 if it is higher. The density of same non-interacting system would be;

$$n(\vec{r}) = \sum_i f_i |\psi_i(\vec{r})|^2 \tag{2.7}$$

this density, by construction, is same as the density of the interacting system. So E_{tot} would include a coulombic term of the form;

$$E_H = \frac{e^2}{2} \int_V \int_V d\vec{r}_2 d\vec{r}_1 \frac{n(\vec{r}_2)n(\vec{r}_1)}{|\vec{r}_1 - \vec{r}_2|} \tag{2.8}$$

External interaction would give;

$$E_{ext} = \sum_i f_i < \psi_i | V_{ext} | \psi_i > \tag{2.9}$$

In practice V_{ext} is the effect of nuclei. If these terms are extracted from the total energy of the interacting system one would get a functional that includes all the many-particle effects. This part of the total energy is known as the exchange-correlation energy of the system

$$E_{xc}[n] = G[n] - E_{ext} - T - E_H \tag{2.10}$$

If $E_{xc}[n]$ was known, the ground state density could be computed by minimizing total ground state energy. This minimization is alone with respect to single-particle wave function $\psi_i(r)$ with the orthogonality constraint;

$$< \psi_i | \psi_j >= \delta_{ij} \tag{2.11}$$

which leads to Kohn-Sham equations;

$$\left[-\frac{1}{2m_e} \nabla^2 + V_H(\vec{r}) + V_{xc}(\vec{r}) + V_{ext}(\vec{r}) \right] \psi_i(\vec{r}) = \epsilon_{ij} \psi_i(\vec{r}) \tag{2.12}$$

The solutions of this equation are used to build up charge density $n(\vec{r})$ in Equation (2.7) in Equation (2.12);

$$V_H(\vec{r}) = e^2 \int_V d\vec{r_1} \frac{n(\vec{r}_1)}{|\vec{r} - \vec{r}_1|} \tag{2.13}$$

and

$$V_{xc}(\vec{r}) = \frac{\delta E_{xc}[n]}{\delta n(\vec{r})} \tag{2.14}$$

The physical observable of KS are total ground-state energy and ground-state charge density.

2.1 The Plane-Wave Pseudopotential Method

In a periodic system, Equation (2.12) can be solved by expanding $\psi_i(\vec{r})$ in a complete set of basis functions, such as plane waves (PW), gaussian functions or atomic orbitals. We will discuss only the plane wave expansion because of its features as simple to use and computational advantages. Because of lattice periodicity, plane waves are natural basis and they don't suffer from basis towards atomic positions. Hartree potential is easier to compute with PW, and one can systematically increase the resolution of the computation by increasing the number of plane waves used to expand $\psi_i(\vec{r})$.

Since $V_{ext}(\vec{r})$ is the nuclear potential, the wave functions if electrons close to nuclei would have highly oscillatory structure, which can be described only huge number of plane waves to get enough acceptable resolutions. From our knowledge, the electrons that important in bonding are valance electrons. And the energies associated with core wave functions are orders of magnitude higher than the energies associated with the valance wave functions. In this case one can eliminated the core electrons which are tightly bond to the nuclei, from Equation (2.12); then can use valance electrons only in stead of the all-electrons as a equivalent cases.

This approximation amounts to substitution of nuclear potential with a pseudopotential whose lowest energies coincides with the valence all-electron energies and whose wave-functions coincide with all-electron wave functions in regions far

away from the nucleus.

Pseudopotential theory has been developed to great accuracies in last three decades. In practice, the pseudopotential of nuclei s is written as

$$V_s(\vec{r}) = V_s^{loc}(\vec{r}) + \sum_{i=0}^{l_{max}} V_{s,l}^{nl}(\vec{r}) P_l \tag{2.15}$$

where P_l is the projector

$$P_l f(\vec{r}) = \sum_{m=-l}^{l} f_{lm}(\vec{r}) Y_l^m(\theta, \phi) \tag{2.16}$$

where Y_l^m is the spherical harmonic of singular momentum l and f_{lm} are the expansion coefficients the function $f(\vec{r})$.

2.2 Plane-Wave Solution of Kohn-Sham Equations

Equation (2.12) is a nonlinear differential eigenvalue equation. The plane wave solutions of this equation for a periodic solid with volume V were given in [12]

Define the KS potential as

$$V_{KS}(\vec{r}) = V_{ext}(\vec{r}) + V_H(\vec{r}) + V_{xc}(\vec{r}) \tag{2.17}$$

this potential will be periodic with the periodicity of the Bravais lattice as;

$$V_{KS}(\vec{r} + \vec{R}_\mu) = V_{KS}(\vec{r}) \tag{2.18}$$

so we can apply Bloch's theorem [13] to Equation (2.12) :

$$\psi_i(\vec{r}) = \psi_i(\vec{k}, \vec{r}) = e^{i\vec{k}\cdot\vec{r}} u_i(\vec{k}, \vec{r}) \tag{2.19}$$

where $\vec{k}$ is a vector inside 1^{st} Brillouin zone and $u_i(\vec{k}, \vec{r})$ periodic with the peri-

odicity of the direct lattice:

$$u_i(\vec{k}, \vec{r} + \vec{R}_\mu) = u_i(\vec{k}, \vec{r}) \tag{2.20}$$

If we have N electrons, we would need $\frac{N}{2}$ lowest filled states factor 2 from $\vec{k}$-points inside the 1^{st} Brillouin zone depends on the boundary conditions and it is equal to number of cells in the case of periodic boundary conditions. So number of full bands, N_b, to one half the number of electrons is the unit cell.

If we insert Equation (2.19) into Equation (2.12) we obtain:

$$\left[\frac{1}{2m_e}(-i\nabla + \vec{k})^2 + V_H(\vec{r}) + V_{xc}(\vec{r}) + V_{ext}(\vec{k}, \vec{r})\right] u_i(\vec{k}, \vec{r}) = \epsilon_i(\vec{k}) u_i(\vec{k}, \vec{r}) \tag{2.21}$$

where

$$V_{ext}(\vec{k}, \vec{r}) = e^{-i\vec{k}\cdot\vec{r}} V_{ext}(\vec{r}) e^{i\vec{k}\cdot\vec{r}} \tag{2.22}$$

Equation (2.21) are N_c different equations (N_c is the number of cells of the crystal). Each of these equations can be solved more easily than original Equation (2.12), because $u_i(\vec{k}, \vec{r})$ have the periodicity of the Bravais lattice and it is possible to expand it in plane waves as;

$$u_i(\vec{k}, \vec{r}) = \frac{1}{\sqrt{V}} \sum_G C_{\vec{k}+\vec{G},i} e^{i\vec{G}\cdot\vec{r}} \tag{2.23}$$

where $\vec{G}$ is a reciprocal vector and $C_{\vec{k}+\vec{G},i}$ are the eigenvectors of a linear eigenvalue problem, obtained by inserting Equation (2.23) into Equation (2.21) as;

$$\sum_{\vec{G}_1}\left[\frac{1}{2m_e}|\vec{k}+\vec{G}|^2\delta_{\vec{G},\vec{G}_1}+V_H(\vec{G}-\vec{G}_1)+V_{xc}(\vec{G}-\vec{G}_1)+V_{ext}(\vec{k}+\vec{G},\vec{k}+\vec{G}_1)\right]C_{\vec{k}+\vec{G}_1,i} \quad = \\ = \epsilon_i(\vec{k})C_{\vec{k}+\vec{G},i} \quad (2.24)$$

where

$$n_V(\vec{G}) = \frac{1}{\Omega}\int_\Omega d\vec{r} n_V(\vec{r})e^{-i\vec{G}\cdot\vec{r}} \quad (2.25)$$

and

$$V_H(\vec{G}) = 4\pi e^2\frac{n_V(\vec{G})}{|\vec{G}^2|} \quad (2.26)$$

and $V_{xc}(\vec{G})$ is the Fourier transform of exchange-correlation potential; Ω is the volume of unit cell. The external potential term is;

$$V_{ext}(\vec{k}+\vec{G},\vec{k}+\vec{G}_1) = \frac{1}{V}\int_V d\vec{r}e^{-i\vec{G}\cdot\vec{r}}V_{ext}(\vec{k},\vec{r})e^{i\vec{G}\cdot\vec{r}} \quad (2.27)$$

The practical solution of Equation (2.24) involves a finite basis set. For pseudopotentials the size of basis is determined by the structure of V_{ext}.

Equation(2.24) is an eigenvalue problem and can be solved by standard numerical methods [14] if the number of G vectors in the expansion is low enough. The traditional eigenvalue methods requires N^3 operations [14]. Even for a small system with 1000 plane-waves, the diagonalization process would be 10^9 operations. Furthermore, only the first very few of the eigenvalues and eigenvectors are relevant for most of the calculations. Based on this observations there has been many different attempts to develop iterative algorithms that would depend on N with a power less than 3. The method used in the calculations reported in

this study is direct minimization of the Kohn-Sham total energy functional with a conjugate gradient algorithm. The details of this approach in beyond the scope of this thesis and can be found in [15].

CHAPTER 3

CU-BASED CHALCOPYRITE SEMICONDUCTORS

The ternary I-III-VI_2 chalcopyrites form a large group of semiconductors with diverse structural, electrical and optical properties [16, 17]. One of this class of materials, $CuAlS_2$, is the widest band gap semiconductor (E_g = 3.49 eV at 300 K [18]) crystallizing in chalcopyrite structure and is an important candidate for blue-to-ultraviolet light emitting device applications [19]. Copper based chalcopyrites $Cu(In,Ga)Se_2$ are considered to be a promising class of materials for solar-cell applications with a proven efficiency of 18.8 % [20]. One way of improving the efficiency of these cells is the use of tandem structures. $CuGaSe_2$-$CuInSe_2$ structure with high band gap (E_g) $CuGaSe_2$ (E_g = 1.68 eV) on top of low gap $CuInSe_2$ (E_g = 1.0 eV) would form an ideal couple for tandem photovoltaic applications [21]. Structural, electronic and lattice dynamical properties of both of these materials have been widely studied for last three decades by a number of experimental and theoretical methods. However, there are still inconsistencies among the reported experimental results concerning especially the lattice dynamical properties which were the subject of recent theoretical work for $CuInSe_2$ [22, 23].

As we mentioned before as a fingerprint properties, the study of characteristic phonon frequencies is one of the most important methods for the characterization of strained materials. Pressure dependence of lattice dynamical properties, such as effective charges, phonon frequencies and low frequency dielectric constants provide crucial information about the structure of the material. Elastic properties is a different tool of these type of research. Elastic constants of most of the

chalcopyrite family of semiconductors have not been determined experimentally because of various difficulties in growing single crystals of these compounds [24]. The availability of reliable elastic constant data is an essential prerequisite for any calculation or analysis of the influence of pressure, stress and strain on the properties of crystals and thin epitaxial layers.

The subject of the present work is to use a first principles linear response approach to delineate the lattice dynamical properties, such as Brillouin zone center phonon frequencies, Born effective charge and dielectric permittivity tensors and elastic compliance tensor of chalcopyrite $CuGaSe_2$ and $CuAlS_2$ under hydrostatic pressure. As chalcopyrite structure can be obtained from the zinc-blende structure by simple doubling and small deformations (as detailed in Section 3.2), $CuGaSe_2$ can be considered as a superstructure of ZnSe and electronic as well as lattice dynamical properties of the former could be derived from those of the latter by using a Brillouin zone folding scheme, as a first approximation. In this work, we also provide a comparison of calculated properties for these two materials and comment on the efficiency of the folding approach.

The Brillouin Zone (BZ) center phonon frequencies have been measured by infrared reflectivity [25, 26, 32] and Raman scattering [25, 26, 27, 28, 29] spectroscopies for $CuAlS_2$ and infrared [30, 31, 32, 33] and Raman [34, 35, 36, 37, 38, 39, 40, 41] spectroscopic measurements for $CuGaSe_2$ at ambient as well as elevated pressures. One interesting point about all these reports is the consistency of data for all the measured mode frequencies for $CuAlS_2$, which is not the case for the other Cu-based chalcopyrite semiconductors [42].

3.1 Methodology

The present results have been obtained using the ABINIT code [43], that is based on pseudopotentials and planewaves. It relies on an efficient Fast Fourier Transform algorithm [44] for the conversion of wavefunctions between real and reciprocal space, on the adaptation to a fixed potential of the band-by-band conjugate gradient method [15] and on a potential-based conjugate-gradient algorithm for the determination of the self-consistent potential [45]. The exchange-correlation energy is evaluated in local density approximation (LDA), using Perdew-Wang parametrization [46] of Ceperley-Alder electron-gas data [47].

The pseudopotentials have been generated with FHI98PP code [48]. The details of choice of pseudopotentials were reported before for calculations of $CuInSe_2$ [22], $CuGaS_2$[49] and $CuInS_2$ [50]. The kinetic energy cutoff needed to obtain a convergence better than 0.01 eV for total energy is found to be equal to 45 Ha. Changing cutoff from 40 to 45 Ha changes response quantities less than 1 %. The Brillouin zone is sampled by 12 special k points, which is found to be enough for convergence of static as well as response calculations.

3.2 Atomic Structure and Lattice Properties

The chalcopyrite structure (space group D_{2d}^{12}, No. 122) (Fig. 3.1) can be considered as derived from the cubic zinc-blende structure (space group T_d^2) (Fig. 3.2) by populating one of the face centered cubic sublattice with group VI atoms and other one with equal amounts of group I and III atoms in a regular fashion. In general, I-VI and III-VI bond lengths, denoted by $d_{\mathrm{I-VI}}$ and $d_{\mathrm{III-VI}}$, respectively, are not equal. One consequence of having two different anion-cation bond lengths is a tetragonal distortion characterized by $u = 0.25 + \left(d_{\mathrm{I-VI}}^2 - d_{\mathrm{III-VI}}^2\right)/a^2$ which describes the repositioning of the anions in the $x-y$ plane, a is the lattice constant

in the x or y direction. The second consequence of differing anion-cation bond lengths is a deformation of the unit cell to a length c which is generally different from $2a$. This tetragonal distortion is characterized by the quantity $\eta = c/a$.

Table 3.1: Reduced coordinates of the eight atoms in the chalcopyrite unit cell. The lattice vectors of the unit cell are $\vec{a}_1 = a(1,0,0)$, $\vec{a}_2 = a(0,1,0)$ and $\vec{a}_3 = a(0.5,0.5,0.5\eta)$ and $x = u/2$.

Atom	Coordinates
Cu_1	$(0,0,0)$
Cu_2	$(-0.25,0.25,0.5)$
Al_1/Ga_1	$(0.5,0.5,0.0)$
Al_2/Ga_2	$(0.25,-0.25,0.5)$
S_1/Se_1	$(x,0.125,0.25)$
S_2/Se_2	$(-(0.25+x),-0.375,0.25)$
S_3/Se_3	$(-0.125,(0.25+x),-0.25)$
S_4/Se_4	$(0.375,-x,-0.25)$

The unit vectors of the primitive cell are: $(a,0,0),(0,a,0),(a/2,a/2,\eta a/2)$ and the coordinates of the atoms in reduced coordinates forming the unit cell are displayed in Table 3.1 (also see Fig. 3.3).

Table 3.2: Calculated structural parameters of $CuGaSe_2$ compared to experimental data (a in $a.u.$, η and u are dimensionless).

	This work	Ref.[53]	Ref.[54]	Ref.[55]
a	10.274	10.610	10.619	10.597
η	1.971	1.965	1.963	1.972
u	0.270	0.250	0.255	-

The ground state properties in the pressure free case are obtained by minimization of total energy with respect to the unit cell volume V. This is done by calculating the total energy for a number of fixed η values. For each η and u is determined by minimizing the force on the atoms. The equilibrium volume,

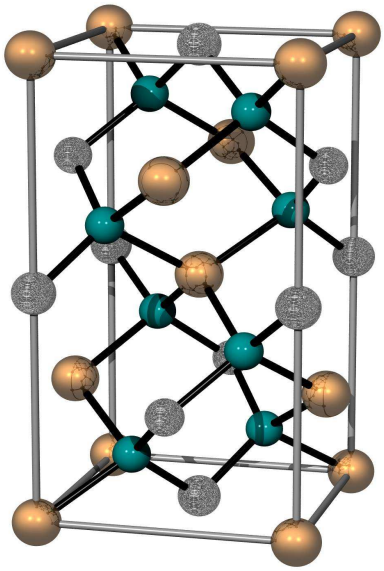

Figure 3.1: Conventional unit cell of chalcopyrite crystal structure. Larger spheres represent cations while the smallest spheres are for anions.

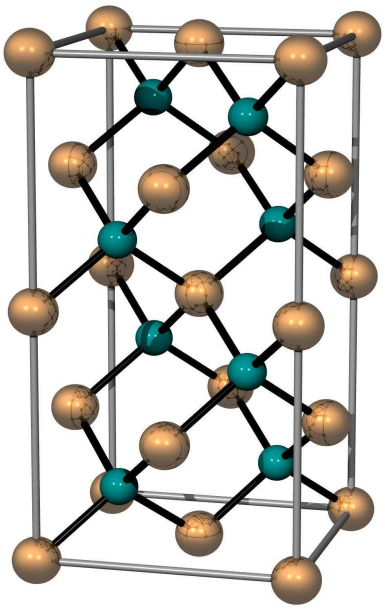

Figure 3.2: Conventional unit cell of zinc-blende crystal structure. Larger spheres represent cations while the smallest spheres are for anions.

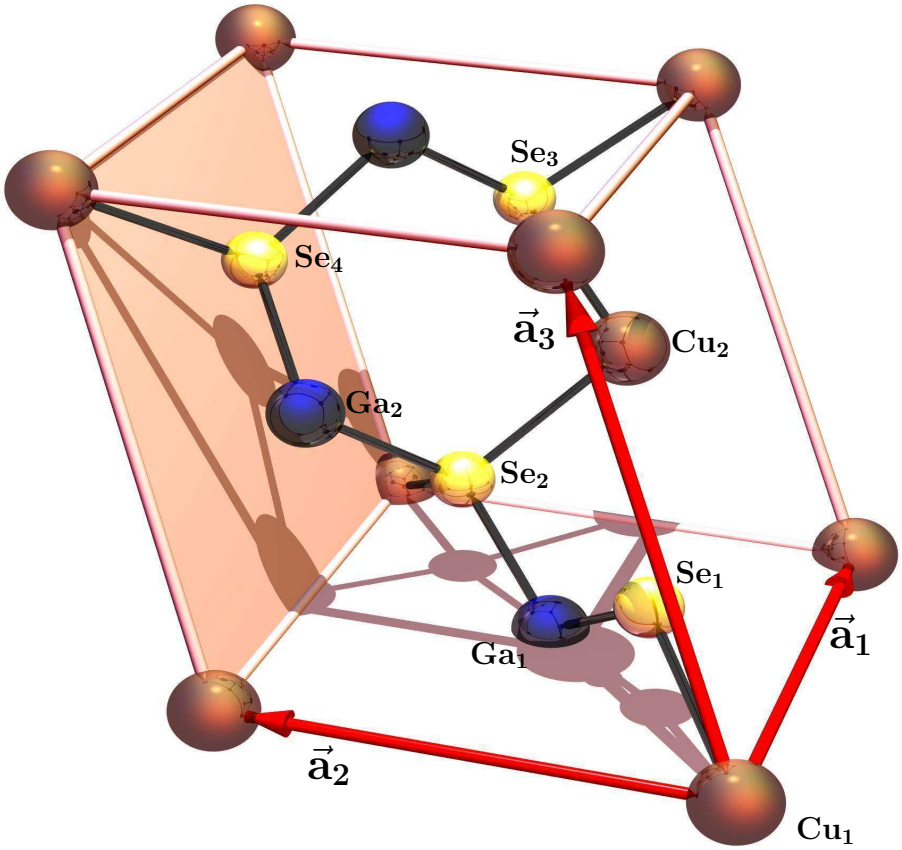

Figure 3.3: Tetragonal chalcopyrite primitive unit-cell.

bulk modulus and its pressure derivatives are calculated by fitting to a third-order Vinet equation of state [56]. The hydrostatic pressure is simulated by a uniform decrease in lattice constants a and c. For each compressed volume u is recalculated from the force considerations.

The zero pressure lattice structural properties are obtained by energy and force minimization and compared to available experimental values in Table 3.2 for $CuGaSe_2$ and in Table 3.3 for $CuAlS_2$. Considering the fact that the zero-point motion and thermal effects are not taken into account, the calculated a, η and u values agree with the experimental values quite well. Since it is found that $u > 0.25$, the Ga-Se bond is slightly shorter than the Cu-Se bond. The bulk modulus and its pressure derivative calculated by fitting to a third-order

Table 3.3: Calculated structural parameters of $CuAlS_2$ compared to experimental data (a in $a.u.$, η and u are unitless).

	This work	Ref.[28]	Ref.[53]	Ref.[57]	Ref.[58]
a	9.900	10.082	10.083	10.043	10.076
η	1.988	1.957	1.958	1.963	1.976
u	0.255	0.255	0.268	-	-

Vinet equation of state [56] are found to be 84.5 GPa and 4.7 which are in good agreement with available experimental bulk modulus values of $CuGaSe_2$ (75.67 [59], 70.18 [60] and 69.31 [61] GPa), but far off compared to the value 57.84 GPa reported by Ref. [62]. ZnSe which is isoelectonic analogue of $CuGaSe_2$ has slightly larger lattice constant $a = 10.7106$ $a.u.$ and lower bulk modulus ($B_0 = 64.7$ GPa) [63]. And the bulk modulus and its pressure derivative of $CuAlS_2$ 97.4 GPa and 4.5 which are in very good agreement with experimental values of 99±3 GPa [27], 94±15 GPa [29], 95.83 GPa [59].

Under pressure tetrahedrally coordinated chalcopyrite compounds undergo transformation to a denser phase with octohedral coordination [64], probably rock-salt structure. The phase transition pressure for $CuGaSe_2$ is around 12.5 GPa [65]. This pressure corresponds to a volume reduction of 15 % if we use our calculated B_0 and B_0' values in Vinet equation of state. Our calculations are done for the volume compression range (up to 10 %) which is far away from the phase transition point.

3.2.1 Elastic Constants

There are a number of ways to calculate the elastic coefficients of a material from first principles. Until recently, the most widely used method was to deform the crystal from its equilibrium shape by a set of tetragonal and sheer deformations

of various sizes and compute the resulting stress by using quantum mechanical definition of stress [66]. Relationships between the applied strain and the calculated stress components provides a set of over-determined linear system which are solved by singular value decomposition to obtain sought elastic stiffness constants. Recently, Hamann *et. al.* [67] developed a reduced coordinate metric tensor method for linear response formulation of strain type perturbations which could be calculated in DFPT. The elastic constants reported in this paper are obtained by the method of Ref. [67] as implemented in Abinit.

Table 3.4: Elastic constants of $CuGaSe_2$ in units of GPa.

		C_{11}	C_{12}	C_{13}	C_{33}	C_{44}	C_{66}
$CuGaSe_2$	This work	112.2	66.4	68.1	113.2	48.4	48.5
$CuInSe_2$	This work	96.8	60.9	63.2	97.0	39.1	37.9
$CuInSe_2$	Ref. [68](Exp.)	97.0	59.7	86.0	108.9	36.2	31.6
$CuInSe_2$	Ref. [69](Theo.)	71.0	45.3	45.3	63.3	45.5	47.4

The elastic stiffness tensor of chalcopyrite compounds has six independent components because of the symmetry properties of D_{2d}^{12} space group, namely $C_{11},\ C_{33},\ C_{44},\ C_{66},\ C_{12},\ C_{13}$ in Young notation. The elastic compliance tensor elements of $CuGaSe_2$ which are calculated by using the method of metric tensor formulation of Hamann [67] are displayed in Table 3.4. Elastic stiffness tensor components must satisfy certain relations known as Born stability criteria [70] which for the tetragonal chalcopyrite lattice requires that $C_{11}, C_{33}, C_{44}, C_{66} > 0$, $C_{11} > |C_{12}|$, $C_{11}C_{33} > C_{13}^2$, $(C_{11} + C_{12})C_{33} > 2C_{13}^2$. The values reported in Table 3.4 satisfy all of these constraints. Since the experimental values are not available for $CuGaSe_2$, to give an idea about the expected experimental-theoretical spread, we display experimental, theoretical and our calculated values for $CuInSe_2$ in the same table. Except for C_{13} ($\approx$25 % underestimated) and C_{66}

(≈20 % overestimated), the agreement between the calculated and experimental values is very good. The results obtained in this work seems to be much closer to the experimental values compared to those reported in Ref. [69]. The main ingredients of calculations in this work and Ref. [69] are similar, namely pseudopotential LDA-DFT. Although the method of elastic constant calculations are different, results should converge to a common value. The pronounced difference in the results of these two sets of calculations might be due to lack of enough convergence in the calculations reported in Ref. [69]. Elastic constants reported in Table 3.4 shows that $CuGaSe_2$, also, displays pseudocubic elastic behavior: for cubic crystals $C_{11}/C_{33} = C_{44}/C_{66} = C_{12}/C_{13} = 1$, from Table 3.4 we find $C_{11}/C_{33} = 0.99,\ C_{44}/C_{66} = 1.00,\ C_{12}/C_{13} = 0.98$ for $CuGaSe_2$. A similar behavior, which is an expected result because of the u and η deformations being so small, was found for other Cu based chalcopyrites in Ref. [69].

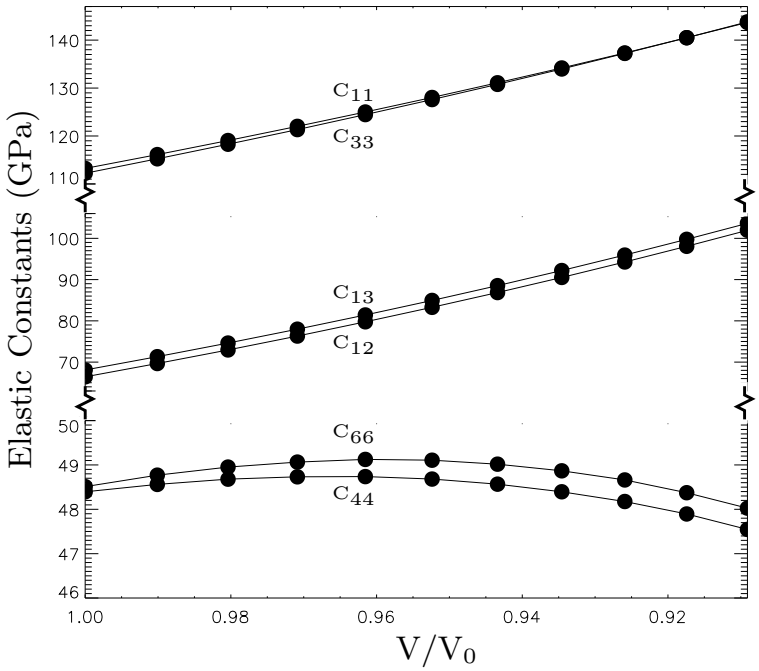

Figure 3.4: Volume dependence of the components of elastic stiffness components of $CuGaSe_2$.

The volume dependence of elastic constants is displayed in Fig. 3.4. As can be seen from the figure, C_{44} and C_{66} increase linearly near zero pressure and then decrease almost linearly at higher pressures while the other elastic tensor components increase with the compression of the lattice. Although the pressure dependence of elastic constants of $CuGaSe_2$ is not available experimentally, elastic constants of a similar compound $CdGaAs_2$ show similar properties at low pressures [24]. Comparing the pressure behavior of elastic constants of $CuGaSe_2$ with those of its binary electronic analog ZnSe, we find a similar trend. Our calculated $P = 0$ pressure derivatives $dC_{11}/dp = 3.74$, $dC_{33}/dp = 4.00$, $dC_{12}/dp = 4.00$, $dC_{13}/dp = 3.58$, $dC_{44}/dp = 0.21$ and $dC_{66}/dp = 0.32$ are comparable to the similar experimental values of $dC_{11}/dp = 4.77$, $dC_{12}/dp = 4.44$ and $dC_{44}/dp = 0.43$ for ZnSe. An interesting point that can be observed from the pressure dependent C_{ij}s is that after a volume reduction of 8%, dC_{44}/dp and dC_{66}/dp become negative. This behavior is also observed for the C_{44} component of ZnSe and is thought to be related to the structural phase transition. As it also can be observed from the figure, reduction of the cubic symmetry of the zinc-blende to tetragonal symmetry of chalcopyrite structure increases the number of independent coefficients of the elasticity tensor from three to six. However, because of the smallness of tetragonal distortion the splittings of $C_{11} - C_{33}$, $C_{12} - C_{13}$ and $C_{44} - C_{66}$ are very small.

One can define linear compressibilities for the pressure response of lattice constants a (κ_a) and c (κ_c) axis of chalcopyrite structure [24]. κ_a and κ_c can be expressed in terms of elastic stiffness constants as:

$$\begin{aligned} \kappa_a &= -\frac{1}{a}\frac{\partial a}{\partial p} = \frac{C_{33} - C_{13}}{C_{33}(C_{11} + C_{12}) - 2C_{13}^2} \\ \kappa_c &= -\frac{1}{c}\frac{\partial c}{\partial p} = \frac{C_{11} + C_{12} - 2C_{13}}{C_{33}(C_{11} + C_{12}) - 2C_{13}^2} \end{aligned}$$

Our calculated κ_a and κ_c are close with values 4.1 and 3.9 TPa^{-1}, respectively. This finding partly justifies treating the effect of hydrostatic pressure on the lattice as uniform contraction of both a and c axis. Volume compressibility, which is defined as $\kappa = 2\kappa_a + \kappa_c$, is equal to 12.1 TPa^{-1} which is similar to that reported for other chalcopyrite compounds [24].

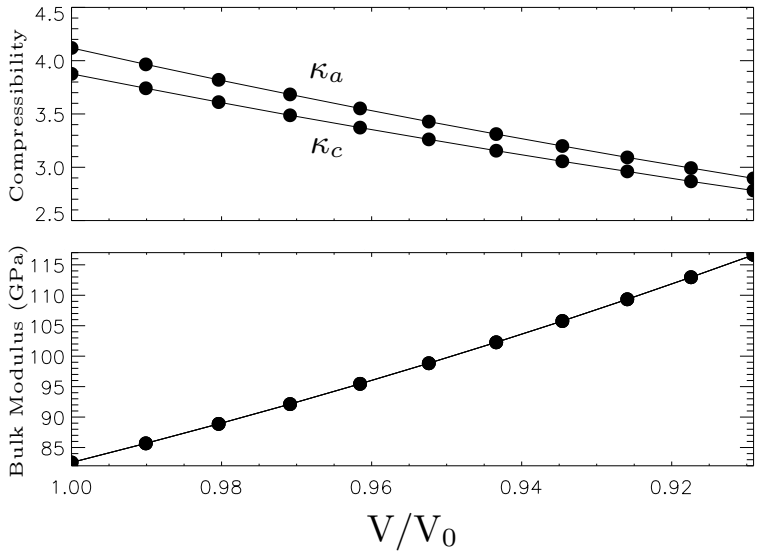

Figure 3.5: Volume dependence of the bulk modulus and a and c axis compressibilities of $CuGaSe_2$.

The volume dependence of κ_a and κ_c and the bulk modulus are displayed in the Fig. 3.5. As expected, compressibilities along the a and c axis decrease linearly with pressure while the bulk modulus increases.

3.3 Born Effective Charges

Born effective charge tensors determine, with the electronic permittivity tensor ϵ_∞, the strength of Coulomb interaction which is responsible for the splitting between the transverse (TO) and the longitudinal (LO) optical modes for insulators. It is a measure of the change in electronic polarization due to ionic displacements. For atom κ, $Z^\star_{\kappa,\beta\alpha}$, quantifies, to linear order, the polarization per unit cell, cre-

ated along the direction β when the atoms of sublattice κ are displaced along the direction α, under the condition of zero electric field. Computationaly, its the mixed second derivative of the total energy with respect to macroscopic field component E_α and β component of the displacement of κth particle.

Table 3.5: Calculated Born effective charges of $CuGaSe_2$. The eigenvalues, λ of the symmetric part of $Z^\star$ are given in brackets. The last column is the Grüneisen parameter, $\gamma^\star$ for the effective charge.

		λ	$\gamma^\star$
$Z^\star_{\mathrm{Cu}}$	$\begin{pmatrix} 0.72 & 0.12 & 0.00 \\ -0.12 & 0.72 & 0.00 \\ 0.00 & 0.00 & 0.64 \end{pmatrix}$	$\begin{bmatrix} 0.72 \\ 0.72 \\ 0.64 \end{bmatrix}$	$\begin{bmatrix} -3.58 \\ -3.58 \\ -3.64 \end{bmatrix}$
$Z^\star_{\mathrm{Ga}}$	$\begin{pmatrix} 2.47 & 0.12 & 0.00 \\ -0.12 & 2.47 & 0.00 \\ 0.00 & 0.00 & 2.72 \end{pmatrix}$	$\begin{bmatrix} 2.47 \\ 2.47 \\ 2.72 \end{bmatrix}$	$\begin{bmatrix} -0.14 \\ -0.14 \\ -0.38 \end{bmatrix}$
$Z^\star_{\mathrm{Se_1}}$	$\begin{pmatrix} -1.41 & 0.00 & 0.00 \\ 0.00 & -1.78 & 0.68 \\ 0.00 & 0.75 & -1.68 \end{pmatrix}$	$\begin{bmatrix} -2.45 \\ -1.41 \\ -1.01 \end{bmatrix}$	$\begin{bmatrix} -0.80 \\ -0.77 \\ -1.54 \end{bmatrix}$
$Z^\star_{\mathrm{Se_3}}$	$\begin{pmatrix} -1.78 & 0.00 & 0.68 \\ 0.00 & -1.41 & 0.00 \\ 0.75 & 0.00 & -1.68 \end{pmatrix}$	$\begin{bmatrix} -2.45 \\ -1.41 \\ -1.01 \end{bmatrix}$	$\begin{bmatrix} -0.80 \\ -0.77 \\ -1.54 \end{bmatrix}$

In Table 3.5 and Table 3.6, we display dynamical effective charge tensors, eigenvalues of symmetric parts of these tensors and Grüneisen parameters of these eigenvalues, $\gamma^\star$ which is defined as

$$\gamma^\star = -\frac{d\ln\lambda}{d\ln V} \tag{3.1}$$

where V is the unit cell volume and λ is the eigenvalue of the symmetric part of relevant effective charge tensor. The effective charge tensors are also displayed graphically in Fig. 3.6. Because of finite k-point sampling there is a deviation

Table 3.6: Calculated Born effective charges of $CuAlS_2$. The eigenvalues, λ of the symmetric part of $Z^\star$ are given in brackets. The last column is the Grüneisen parameter, $\gamma^\star$ for the effective charge.

		λ	$\gamma^\star$
$Z^\star_{\mathrm{Cu}}$	$\begin{pmatrix} 0.59 & -0.10 & 0.00 \\ 0.10 & 0.59 & 0.00 \\ 0.00 & 0.00 & 0.57 \end{pmatrix}$	$\begin{bmatrix} 0.59 \\ 0.59 \\ 0.57 \end{bmatrix}$	$\begin{bmatrix} -3.73 \\ -3.73 \\ -3.59 \end{bmatrix}$
$Z^\star_{\mathrm{Al}}$	$\begin{pmatrix} 2.61 & -0.05 & 0.00 \\ 0.05 & 2.61 & 0.00 \\ 0.00 & 0.00 & 2.66 \end{pmatrix}$	$\begin{bmatrix} 2.66 \\ 2.61 \\ 2.61 \end{bmatrix}$	$\begin{bmatrix} -2.23 \\ -2.23 \\ -0.01 \end{bmatrix}$
$Z^\star_{\mathrm{S_1}}$	$\begin{pmatrix} -1.53 & 0.00 & 0.00 \\ 0.00 & -1.67 & 0.62 \\ 0.00 & 0.63 & -1.61 \end{pmatrix}$	$\begin{bmatrix} -2.27 \\ -1.53 \\ -1.01 \end{bmatrix}$	$\begin{bmatrix} -0.62 \\ -0.52 \\ -1.31 \end{bmatrix}$
$Z^\star_{\mathrm{S_3}}$	$\begin{pmatrix} -1.67 & 0.00 & 0.62 \\ 0.00 & -1.53 & 0.00 \\ 0.63 & 0.00 & -1.61 \end{pmatrix}$	$\begin{bmatrix} -2.27 \\ -1.53 \\ -1.01 \end{bmatrix}$	$\begin{bmatrix} -0.62 \\ -0.52 \\ -1.31 \end{bmatrix}$

from charge neutrality which is less than 0.01 electron for the unit cell. The first thing to consider from Table 3.5 is that compared to nominal charges of Cu, Ga, and Se in $CuGaSe_2$ (+1, +3 and −2 respectively), the dynamical charges show no anomalous behavior which is expected because such anomalous effective dynamical charges are observed for ferroelectricity unstable semiconductors as well as near metallic and strongly-correlated electronic systems [71] and $CuGaSe_2$ has none of these properties. A similar trend is observed for the other $CuXY_2$ chalcopyrites where X=Al, Ga, In and Y=S and Se.

The form of effective charge tensor for the constituents is determined by the site symmetry of the ions. $Z^\star$ of cations, which have same site symmetry (they are located at $4a$ and $4b$ Wyckoff positions) are almost diagonal with an anisotropy of ≈12.5% for Cu and ≈-9.2% for Ga for $CugaSe_2$. These anisotropies are higher than those seen in $CuAlS_2$ as 4% for Cu and 2% for Al, but still low enough that

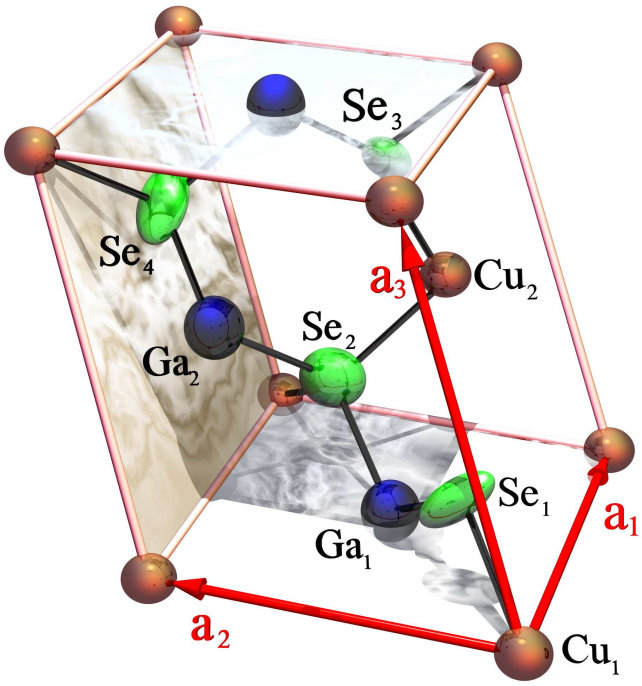

Figure 3.6: Dynamical Born effective charges of chalcopyrite $CuGaSe_2$. Here, for each atom the unit sphere is transformed by the effective charge tensor of that atom. Ga and Se spheres are further scaled by 1/3 and 1/2, respectively for visual clarity.

the shapes of Cu and Ga in Fig. 3.6 are still almost spherical. The shape of $Z^\star$ for Se ion is markedly different from that of cations as can be seen from Table 3.5 and Fig. 3.6. Se and S ions are located at lower symmetry sites ($8d$ positions) and as a result their effective charge tensors have nonequivalent diagonal components as well as sizable off-diagonal components. The tetrahedral shifting of anion atoms creates four different configurations for these atoms and the resulting effective charge tensor elements can be divided into two classes according to the direction of the tetrahedral shifting being along x or y direction. $Z^\star_{\mathrm{Se},zz} = -1.68$ for all anions while $Z^\star_{\mathrm{Se},xx}$ and $Z^\star_{\mathrm{Se},yy}$ take the value -1.41 or -1.78 depending on the direction of u and same behavior $Z^\star_{\mathrm{S},zz} = -1.61$ for all anions while $Z^\star_{\mathrm{S},xx}$ and $Z^\star_{\mathrm{S},yy}$ take the value -1.53 or -1.67 depending on the direction of u. Also, depending

on the u distortion being along x or y direction, the off-diagonal components $Z^{\star}_{\mathrm{Se},zx}, Z^{\star}_{\mathrm{Se},xz}$ or $Z^{\star}_{\mathrm{Se},yz}, Z^{\star}_{\mathrm{Se},zy}$ and $Z^{\star}_{\mathrm{S},zx}, Z^{\star}_{\mathrm{S},xz}$ or $Z^{\star}_{\mathrm{S},yz}, Z^{\star}_{\mathrm{S},zy}$ are different than zero. Hence, the shape of effective charge tensor for anions is far from being spherical, which also has been observed for other members of the Cu-based chalopyrite family of semiconductors.

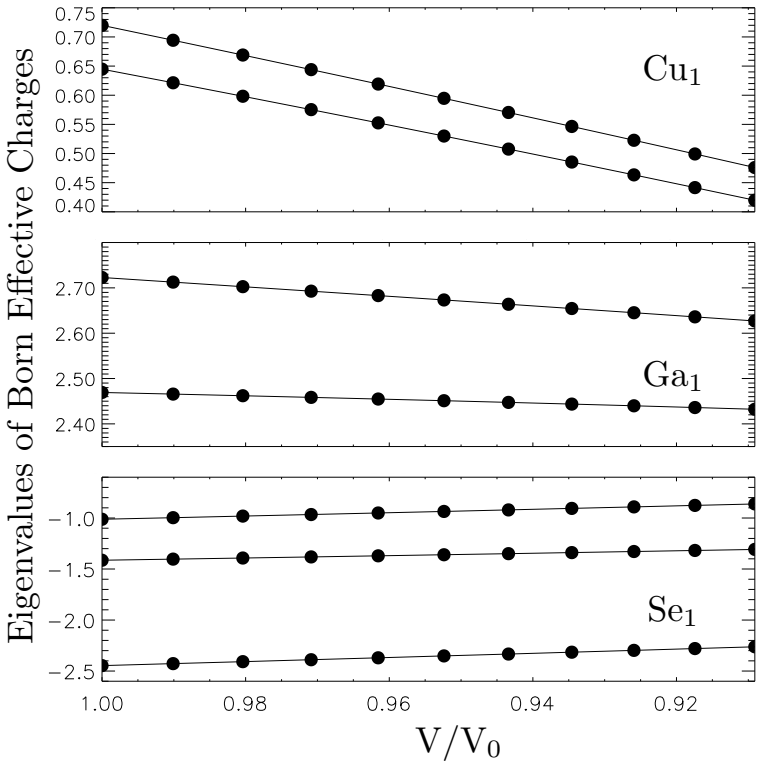

Figure 3.7: Volume dependent Born effective charges of $CuGaSe_2$.

As can be seen from the Table 3.5 and Table 3.6, the Grüneisen parameter for the dynamical effective charges of all the ions are negative, which indicate that $Z^{\star}$ decreases with increasing pressure. The eigenvalues of the symmetric part of the effective charge tensors are displayed as function of the volume in Fig. 3.7. The most important conclusion from the effective charge Grüneisen parameters in Table 3.5 and Table 3.6 and the graphs in Fig. 3.7 is that the Born effective charges decrease linearly with pressure in the considered pressure range. Pressure induced reduction of effective charges indicates a charge redistribution

in comparison with zero pressure situation is found to be the case for almost all zinc-blende materials, except SiC [72].

3.4 Dielectric Permitivity Tensors

The form of the dielectric tensor is determined by the symmetry of the crystal. Our calculated electronic (ϵ_∞) and static (ϵ_0) dielectric tensors have two independent components $\epsilon^{||}$ and $\epsilon^{\perp}$ along and perpendicular to the c axis, respectively. We display our calculated dielectric tensor components along with model calculations of Ref. [73] and experimentally available values in Table 3.7 and Table 3.8. The averages of ϵ_∞ and ϵ_0, obtained from the expression ϵ_∞ (or ϵ_0)$= (2\epsilon_\infty^{\perp} + \epsilon_\infty^{||})/3$ are also shown in these tables. While electronic dielectric tensor is almost isotropic, ϵ_0 has a small ($\approx 4.0\%$, $\approx 2.8\%$ for $CuGaSe_2$ and $CuAlS_2$ respectively) anisotropy, which is consistent with the fact that for $CuGaSe_2$ and $CuAlS_2$ tetragonal distortion is very small ($\eta = c/a \approx 2$).

Table 3.7: Static and high frequency dielectric tensor components of $CuGaSe_2$.

	$\epsilon_\infty^{||}$	$\epsilon_\infty^{\perp}$	ϵ_∞	$\epsilon_0^{||}$	$\epsilon_0^{\perp}$	ϵ_0
This work	9.19	9.32	9.28	11.31	10.86	11.01
Ref.[31]	4.75	6.50	5.92	6.08	8.45	7.66
Ref.[32]	4.2	5.1	4.8	6.31	7.4	7.04
Ref.[33]	4.20	5.13	4.82	7.30	12.86	11.01
Ref.[73]	6.6	6.8	6.7	9.5	9.7	9.6
Ref.[33][1]	8.11	7.17	7.48	12.38	14.40	13.73

[1]Refitted Ref.[33] data.

The experimental infrared data for the electronic part of the dielectric tensor of $CuGaSe_2$ are similar and around 5, but for the static $\epsilon_0^{\perp}$ component there is $\approx$ 50 % difference between the values reported in Ref. [31] and Ref. [33]. We

Table 3.8: Static and high frequency dielectric tensor components of $CuAlS_2$.

	$\epsilon_\infty^\parallel$	$\epsilon_\infty^\perp$	ϵ_∞	$\epsilon_0^\parallel$	$\epsilon_0^\perp$	ϵ_0
This work	6.81	6.94	6.85	8.84	8.59	8.76
Ref.[25]	4.9	5.0	5.0	6.7	6.4	6.5
Ref.[32]	4.80	4.90	4.87	7.05	8.14	7.68
Ref.[73]	5.1	5.2	5.2	6.9	7.0	7.0

have performed a refitting of the reflectance data of Ref. [33] and found that the dielectric tensor components displayed in the last row of Table 3.7 would provide a much better fit. It should be noted that these values are obtained by fitting to the sum form of the model dielectric function which is the same form as used in Ref. [33]. We have found that an even better fit can be obtained by using the product form of model dielectric function with similar ϵ_∞ components. As can be seen from Table 3.7, our electronic computed dielectric components agree the most with the refitted values derived from the infrared reflectance data of Ref.[33]: our theoretical ϵ_∞ values are $\approx$ 15 % higher than the experimental values. The overestimation of the calculation is a well-known artifact of the density functional theory (DFT) which is related to underestimation of the band-gap in DFT[74, 75, 76].

Similar to that of Born effective charges, one can define a dielectric Grüneisen parameter

$$\gamma^\epsilon = -\frac{d\ln\epsilon}{d\ln V} \tag{3.2}$$

to characterize the pressure dependence of the dielectric constants. For $CuGaSe_2$, we have found that the perpendicular and parallel components of $\gamma^{\epsilon\infty}$ are both negative with a similar Grüneisen parameter ($\gamma^{\epsilon_\infty^\parallel}$=-0.390, $\gamma^{\epsilon_\infty^\perp}$=-0.372) which is similar to $\gamma^{\epsilon\infty}$ for zinc-blende compounds[72]. And We have found for $CuAlS_2$,

γ^{ϵ_∞}, to be very small negative($\gamma^{\epsilon_\infty^{\parallel}}$=-0.0046) for $\gamma^{\epsilon_\infty^{\parallel}}$ and small positive ($\gamma^{\epsilon_\infty^{\perp}}$=0.0081) for $\epsilon_\infty^{\perp}$ components. This is surprising, because γ^{ϵ_∞} for zinc-blende compounds is much larger than these values[72].

The Grüneisen parameters for the components of static dielectric function ϵ_0 are also all negative with higher absolute values compared to those of high frequency components ($\gamma^{\epsilon_0^{\perp}}$=-0.731, $\gamma^{\epsilon_0^{\parallel}} = -0.811$, γ^{ϵ_0}=-0.784) for $CuGaSe_2$ and ($\gamma^{\epsilon_0^{\perp}}$=-0.50, $\gamma^{\epsilon_0^{\parallel}} = -0.38$, γ^{ϵ_0}=-0.46) for $CuAlS_2$. These values are also around those values reported for zinc-blende compounds[72].

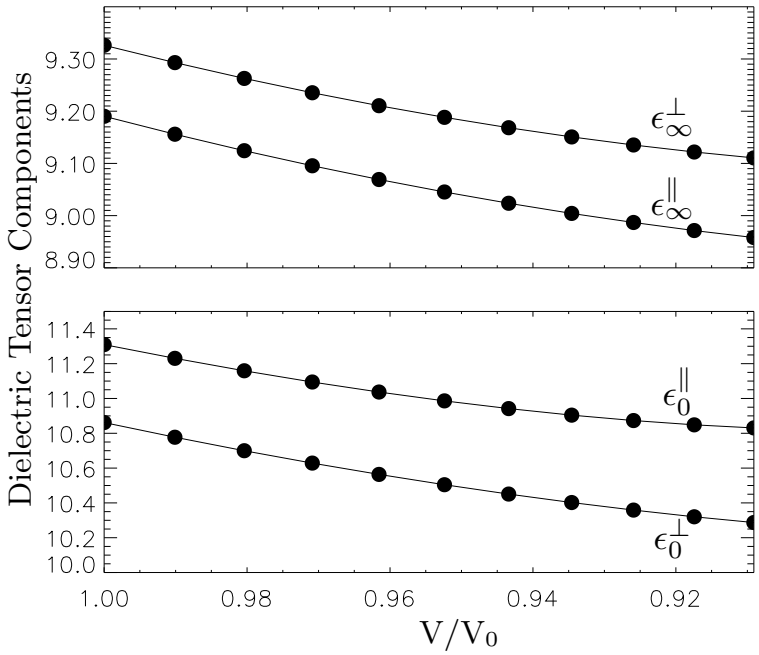

Figure 3.8: Volume dependent static and high frequency dielectric tensor components of $CuGaSe_2$.

Figure 3.8 displays our calculated volume-dependent static and high frequency dielectric tensor components. All of the components decrease under pressure; the volume dependence of static (high-frequency) components is slightly (highly) nonlinear, especially at higher pressures, which is similar to what has been found for the most tetrahedrally coordinated semiconductors.

3.5 Zone Center Phonons

The unit cell of the chalcopyrite structure is almost twice the volume of zinc-blende one, with the Brillouin zone being four times smaller than that of the cubic structure. As a result, Γ, X and W symmetry points of zinc-blende Brillouin structure zone fold to Γ of the chalcopyrite structure. Since the body-centered tetragonal primitive unit cell of the chalcopyrite structure has eight atoms (see Fig.3.6), the number of vibrational modes for this structure is 24. A detailed discussion of group theoretical properties of chalcopyrite zone center phonons can be found in Refs.[6]. The irreducible representation at the center of the Brillouin zone is

$$\Gamma_{\text{aco}} = 1\Gamma_4 \oplus 1\Gamma_5$$

for acoustic modes, and

$$\Gamma_{\text{opt}} = 1\Gamma_1 \oplus 2\Gamma_2 \oplus 3\Gamma_3 \oplus 3\Gamma_4 \oplus 6\Gamma_5$$

for optical modes. Optical modes having Γ_1 and Γ_2 symmetry involve only displacement of cations. Γ_3, Γ_4 and Γ_5 modes include displacement of anions, as well. Both Γ_4 and Γ_5 modes belong to vector transforming representation, and are thus IR active. Inclusion of the long range polarization interaction results in splitting of the Γ_4 and Γ_5 modes into TO and LO components giving nine polar vibrations (three with polarization along c (Γ_4 modes) and six along x or y (Γ_5)). This results in different numbers of IR modes being active for $E \| c$ and $E \perp c$. Except modes of Γ_2 symmetry, all optical modes are Raman active.

The infrared active Γ_4 mode involves in-phase motion of each cation pair and that of two anion pairs along the principal axis and as a result has a dipole

moment in that direction. For the infrared active Γ_5 mode, the resultant motion of each cation pair and that of each anion pair are along either of x and y axis which causes twofold degeneracy and a dipole moment in the $x-y$ plane. Γ_1 and Γ_3 modes are out of phase motion of ions and they do not have a dipole moment, so they are Raman active but not infrared active. Γ_2 mode is out-of-phase motion of anion pairs and does not produce a dipole moment.

In Table 3.9 and Table 3.10 our calculated zone center phonon frequencies of $CuGaSe_2$ and $CuAlS_2$ respectively. Their symmetry assignments and mode Grüneisen parameters are displayed and compared with infrared [30, 31, 32, 33] and Raman [34, 35, 36, 37, 38, 39, 40, 41] spectroscopic measurements for $CuGaSe_2$ and infrared [25, 26, 32] and Raman [25, 26, 27, 28] spectroscopic measurements for $CuAlS_2$. Among the experimental phonon frequencies Raman data of Ramirez *et. al.*[37] and Gonzalez *et. al.*[38] and infrared data of Syrbu *et. al.*[33] are the most complete sets of $CuGaSe_2$ zone center phonon frequencies. The zone center phonon frequencies of Cu-based chalcopyrite semiconductors, generally, are clearly grouped into three groups: low, medium and high frequency. As can be seen from Table 3.9 for $CuGaSe_2$ these groups are low:65-97 cm^{-1}, medium:170-223 cm^{-1} and high:265-295 cm^{-1}. Γ_1 mode which involves the motion of only the anions is always the strongest line observed in the Raman scattering of Cu-based chalcopyrite compounds and because of that its frequency well-established for $CuGaSe_2$ in the range 182-187 cm^{-1} which can be seen from the Table 3.9. Our calculated value for this mode is 197 cm^{-1} which is in good agreement with the experimental values. Although there are some discrepancies among the experimental data for almost every mode with the exception of Γ_1 mode, the most problematic values seem to be the Raman results of Ref.[37] for the high frequency Γ_3 modes. Our calculated frequencies and Raman mea-

surements reported by Ref.[38] coupled with the results of experimental as well as computational studies on other Cu-based chalcopyrites seem to indicate that each one of three Γ_3 mode frequencies should be in the low, medium and high frequency region. The discrepancies among experimental Γ_4 and Γ_5 mode frequencies are relatively low compared to some other Cu-based chalcopyrites and our calculated frequencies show reasonable agreement with the available values. $CuAlS_2$ is rather interesting among the Cu-based semiconductors that crystallize in chalcopyrite structure, because, contrary to other members of this family [42, 22, 49, 69], reports of its zone-center phonon frequencies agree well with each other. As can be seen from the Table 3.10, based on relative root-mean square (rms) deviation values, our calculated mode frequencies agree very well with the experimental results, especially low temperature Raman measurements reported by Bairamov *et. al.* [28]. Except for Andrish *et. al.*'s infrared data [32], all the rms deviations between our calculated results and the experimental data are within the range of expected accuracy of DFT response calculations.

The calculated LO-TO mode splitting of Γ_4 and Γ_5 modes of $CuGaSe_2$ are small, ranging from 0 to 20 cm^{-1}. As can be observed from the Table 3.9, the highest splitting is for the highest frequency modes for both symmetries which is also the case for the experimental data. The small and even zero splitting for the low frequency modes can be traced back to the origin of these modes: since the low frequency modes are essentially the folded acoustic modes, they correspond to whole molecular units moving relative to each other. On the other hand, the high frequency modes involve individual atoms moving against each other which produces higher dipole moments which lead to higher splitting. The highest of these splitting values are around the half of the LO-TO splitting for zone center optical mode of isoelectronic ZnSe. A similar reduction value was obtained by

Lambrect *et. al.*[77] who compared the splittings for ternary $ZnGeN_2$ and its isoelectronic analog binary GaN.

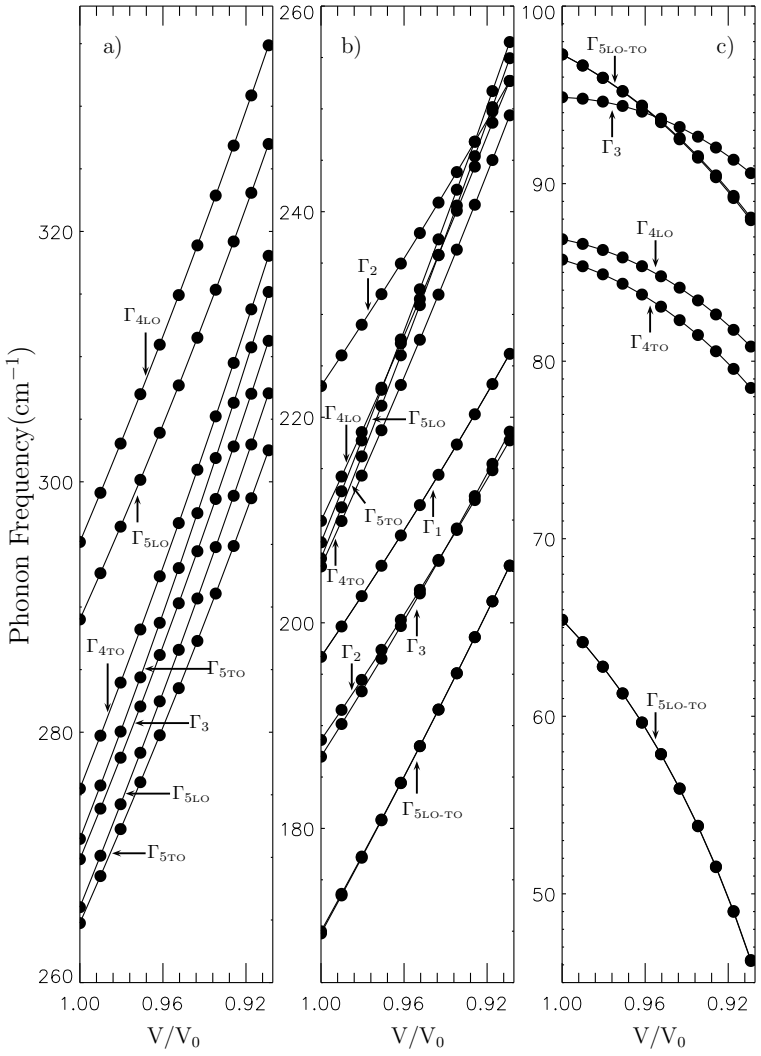

Figure 3.9: Volume dependence of phonon frequencies for $CuGaSe_2$ at the Γ point.

The hydrostatic pressure dependence of phonon mode i with frequency ω_i is characterized by the Grüneisen parameter γ_i which is defined as

$$\gamma_i = -\frac{d \ln \omega_i}{d \ln V} \tag{3.3}$$

where V is the unit cell volume of the crystal. In Table 3.9 and Table 3.10, we also display our calculated mode Grüneisen parameters. To best of our knowl-

edge, there are no reported experimental Grüneisen parameters for the Γ point phonons of $CuGaSe_2$. Here we discuss the computed results with reference to γ_is of comparable compounds. One of the interesting properties of phonons of tetrahedrally coordinated semiconductors of diamond and zinc-blende structure is the pressure softening of their transverse acoustic (TA) modes. Mode Grüneisen parameter for TA modes of Group IV, III-V and II-VI compounds that crystallize in diamond and zinc-blende structure are all negative towards the Brillouin zone boundaries[9] and this negativity is thought to be the mechanism of structural phase transition of these compounds at elevated pressures. The correspondence between the chalcopyrite zone center phonon modes and modes in zinc-blende structure has been given in Refs.[78, 6, 7, 8]. We have found three negative mode Grüneisen parameter for $CuGaSe_2$, which are two low frequency optical Γ_5 and one low frequency Γ_4 modes and we have found three negative mode Grüneisen parameter for $CuAlS_2$, which are two low frequency optical Γ_5 and one low frequency Γ_4 modes. These modes originate from X_{5ac}, W_{4ac} and W_{2ac} modes of zinc-blende structure, respectively. γ for the X_{5ac}-originated mode is similar in magnitude and sign to values reported for zinc-blende structures [79, 80, 81, 82]. Frequency and mode Grüneisen parameters at W point for zinc-blende materials are, unfortunately, not as well known as those at X point. From the available data [79] we would expect a smaller, but still negative Grüneisen parameter. Experimental γ for these two modes seem to be very small but positive.

For zinc-blende materials, the mode Grüneisen parameter for longitudinal optical phonon modes (γ_{TO}) is generally higher than that of transverse optical mode (γ_{LO}) [79], which is interpreted as reflection of a decrease in ionicity with increasing pressure. We have found a similar relationship for $CuGaSe_2$ for the polar modes (the highest frequency Γ_5 and Γ_4 modes) originating from the zone-

center polar mode (Γ_{15}) of zinc-blende structure.

The volume dependent zone center phonon frequencies of $CuGaSe_2$ are shown in Fig. 3.9. High and intermediate frequency modes, which are displayed in Fig. 3.9a and Fig. 3.9b respectively, show a similar volume dependence; their frequency increase linearly with pressure at different rates.

Table 3.9: Frequencies of phonons of $CuGaSe_2$ and mode Grüneisen parameters at the Γ point (ω in cm^{-1}). All experimental data, except those indicated in the footnote, are room temperature measurements.

	Ab initio	Experiment													γ_i
Mode	Present	IR[30]	IR[31]	IR[32]	IR[33]	R[41]	R[41][1]	R[35]	R[36]	R[37]	R[38]	R[34]	R[39]	R[40]	Present
Γ_1	197					187	188	188	184	180,185	183	182	185	187	1.5
Γ_2	223														1.3
Γ_2	189														1.5
Γ_3	270									128,130	263				1.5
Γ_3	187							192	116	108,110	165				1.7
Γ_3	95								96	90,94	76	93			-0.04
Γ^{LO}_{4TO}	295	278	265	273	273	–	–	265	261	259,261	278	–	–	–	1.3
	275	254	244	257	257	–	–	244			252	–	–	–	1.5
Γ^{LO}_{4TO}	210	196	194	188	188	–	–	194	199	200,202	–	–	195	199	2.1
	205	178	186	177	177	–	–	186			187	–	–	–	2.2
Γ^{LO}_{4TO}	87	–	–	96	96	–	–	60	60	68	98	57	–	–	−0.3
	86	–	–	86	86	–	–	60			98		–	–	−0.4
Γ^{LO}_{5TO}	289	276	269	277	277	274	278	269	261	273	273	269	274	277	1.3
	271	250	241	255	255	249	252	241			–		–	253	1.6
Γ^{LO}_{5TO}	266	–	–	186	186	–	–	–	239	237,245	243	267	227	242	1.5
	265	–	–	180	180	–	–	–			219		–	238	1.4
Γ^{LO}_{5TO}	208	190	188	149	149	–	193	188	–	153,156	187	242	153	–	2.4
	206	170	184	145	145	–	–	184	–		170	–	–	193	2.4
Γ^{LO}_{5TO}	170	–	–	109	135	154	154	–	168	141,142	140	204	–	–	2.1
	170	–	–	105	128	–	–	156			140		–	–	2.2
Γ^{LO}_{5TO}	97	–	–	90.9	91	96	96	–	–	117,121	–	–	80	117	−0.6
	97	–	–	88.2	82	86	86	98	–		–	–	–	–	−0.6
Γ^{LO}_{5TO}	65	–	–	66	67.5	–	–	–	60	75	58	–	60	78	−1.8
	65	–	–	64.5	64	60	59	–			58	–	–	60	−1.8
		rms relative deviations													
		0.114	0.106	0.290	0.238	0.083	0.076	0.187	0.279	0.386	0.144	0.232	0.124	0.038	

[1]Ref.[41] (at 77 K)

Table 3.10: Frequencies of phonons of $CuAlS_2$ and mode Grüneisen parameters at the Γ point (ω in cm^{-1}). All experimental data, except those indicated in the footnote, are room temperature measurements.

	Ab initio	Experiment									γ_i		
Mode	Present	IR[25]	IR[26]	IR[32]	R[25]	R[27]	R [26][1]	R[28]	R [28][2]	R [29]	Present	Ref.[27]	Ref.[29]
Γ_1	325				315	315	316	314	317	315	1.5	1.5	1.6±0.2
Γ_2	366										1.4		
Γ_2	304										1.4		
Γ_3	448					440	443	442	448		1.6	1.4	
Γ_3	263				268	268	269	263	266		0.9	0.7	
Γ_3	115				98	98	102	96			0.8	0.9	
Γ^{LO}_{4TO}	495	498		500	497	495		498	503		1.4	1.1	
	453	446	446	456	445	456	446	446	448		1.7	1.3	
Γ^{LO}_{4TO}	296	284		285	278	270					1.9	2.7	
	287	271	271	264	266	270	267	272	274		1.7	2.7	
Γ^{LO}_{4TO}	120			111	112	111		108			−0.1	0.1	
	119		114	105	112	111	114	108			−0.3	0.1	
Γ^{LO}_{5TO}	489	497	497	496	494	495	499	496	498		1.3	1.1	
	449	444	444	452	445	444	444	444	449		1.7	1.5	
Γ^{LO}_{5TO}	440	432		434		420					1.7	1.5	
	436	432	432	430		373	433				1.5	1.0	
Γ^{LO}_{5TO}	290	266	266	242	265	266	267	263	275		1.8	2.2	
	287	263	263	228	262	266	265	261	265	265	1.9	2.2	1.9 ± 0.3
Γ^{LO}_{5TO}	218	217	217	220	219	220	220	218	220		1.2	0.6	
	218	216	216	208	218	220	218	218	220	218	1.2	0.6	0.8 ± 0.2
Γ^{LO}_{5TO}	146		140			150	142	135			−0.1	0.2	
	146		140			150	142	135			−0.1	0.2	
Γ^{LO}_{5TO}	83		77		76	78	78	76	77		−1.1	−0.6	
	83		77		76	78	78	74	77	76	−1.2	−0.6	≤ ±0.3
		rms relative deviations											
		0.046	0.056	0.103	0.073	0.072	0.056	0.083	0.045	0.062			

[1]Ref.[26] (at 78 K), [2]Ref.[28] (at 8 K)

CHAPTER 4

HIGH DIELECTRIC CONSTANT MATERIALS

Starting with the observation of giant dielectric constant (GDC) in $CaCu_3Ti_4O_{12}$ (CCTO) [83, 10] perovskite-derived oxides with GDC ($\epsilon_0 > 10^3$) have been the subject of many recent studies, in part because of various potential technological applications of the materials with such properties and in part because of the possible origin of the such high dielectric constant. Investigation of the dielectric properties of many compounds of the form $ACu_3Ti_4O_{12}$, where A might be Ca, Cd, $La_{2/3}$, $Na_{1/2}Y_{1/2}$ or $Na_{1/2}Bi_{1/2}$ showed that all of them had large dielectric constants over a wide temperature range ($\sim$ 150-600 K) [11, 84]. Ferrarelli *et. al.* reports room temperature permitivity of over 10000 for $Na_{1/2}Bi_{1/2}Cu_3Ti_4O_{12}$ (NBCTO) and around 10000 for CCTO at 100 kHz [84].

Several mechanisms, both extrinsic and intrinsic, have been advanced to shed light on the origin of the giant dielectric response. The proposed intrinsic mechanisms are related to lattice instability that leads to ferroelectric or relaxor-like behavior. Although no ferroelectric phase is observed in GDC compounds [85], Homes *et. al.* argued that the giant dielectric response might be the result of local dipole moments associated with off-center displacements of Ti atoms [10, 86]. Another intrinsic mechanism is proposed by Ramirez *et. al.* [87] which focuses on the defects in the Ca-Cu sublattice which might disrupt Cu-O complex and leads to local polarizability. Recently, Zhu *et. al.* [88] have shown the existence of a Ca and Cu substitution disorder by using quantitative electron diffraction and extended x-ray absorption fine structure techniques and claimed that the microscopic origin of GDC might be related to this disorder. The proposed extrinsic mechanisms are

related to the morphology of the sample and boundary-layer effects. Sinclair *et al.* attribute the giant dielectric phenomenon to a grain boundary barrier layer capacitance [89, 90] while a number of studies claim a Maxwell-Wagner type source which involves enhancement from the depletion layers at grain boundaries [91, 92].

The first principles investigation of the electronic, magnetic and lattice dynamical properties of GDC compounds, mostly CCTO, have been carried out by a number of groups [93, 94, 96, 97, 95]. Electronic, magnetic and lattice dynamical properties of CCTO and $CdCu_3Ti_4O_{12}$ (CdCTO) were investigated by He *et. al.* [93, 94] within the ultrasoft pseudopotential local spin density approximation framework [93, 94]. He *et. al.*'s work focuses on the lattice dynamical properties and the lattice susceptibility contribution to the static dielectric response and found that there was no unstable phonon mode that might lead to a ferroelectric transition and the lattice contribution to dielectric constant is too low to account for the observed GDC. Electronic and magnetic properties of CCTO were, also, calculated by using the full-potential linearized augmented plane-wave method (FLAPW) within LSDA [96, 97, 95]. Li *et. al.* studied the magnetic structure of CCTO and found that the AFM order is favored over the ferromagnetic and nonmagnetic order. Chen and Wang [98] used local combination of atomic orbital basis in Hartree-Fock (HF) framework to study electronic structure of CCTO and $CaCu_3Mo_4O_{12}$ (CCMO) and found that HF approach was better in determining the energy gap.

The intrinsic bulk permittivity of GDC compounds has been, also, found to be high compared to the value computed from a simple Clausius-Mossotti relation or density functional calculations by a factor of two for CCTO [93] (experimental value ~ 105) and four (experimental value ~ 235) for NBCTO [84]. Grubbs *et. al.* have studied the temperature dependent dielectric and magnetic properties

of Fe-and Nb-doped CCTO and argued that the intrinsic ϵ' could only be due to soft polar TO mode [99].

The aim of these part of the present study is to investigate the origin of dielectric response of $Na_{1/2}Bi_{1/2}Cu_3Ti_4O_{12}$ by using first principles techniques. To this end we have performed detailed DFT and density functional perturbation theory (DFPT) calculations to determine the electronic structure, magnetization density, and lattice dynamical properties such as Born effective charges and Brillouin zone center phonon frequency and eigenvectors that determine the lattice contribution to low frequency dielectric constant.

4.1 Methodology

All the calculations reported here were done with the Abinit [43] package which is an implementation of density functional theory. Abinit uses planewaves for the expansion of electronic wavefunctions and the pseudopotentials for the interaction electrons and the nuclei. We use local spin density approximation for the exchange-correlation kernel as parametrized by Perdew and Wang [46]. All atoms are represented by norm-conserving [100] designed nonlocal [101] pseudopotentials which are created by using the OPIUM code [102]. The Na (2s, 2p, and 3s), Bi (5d, 6s and 6p), Cu (3d, 4s, and 4p), Ti (3s, 3p, 4s, and 3d), and O (2s and 2p) were treated as valence states. And details of valance wavefunctions can be seen graphically in Fig. 4.1-4.5. Lattice dynamical and dielectric properties such as Born effective charges, Brillouin zone center phonon frequencies, and oscillator strength are calculated in the linear response formalism of density functional perturbation theory as implemented in Abinit in terms of iterative minimization techniques which is described by Gonze *et al.* in Refs. [51, 103]. Plane wave kinetic energy cutoff of 40 Ha was found to be enough for the convergence of 1

cm^{-1} in the phonon frequencies . The Brillouin zone integrations were performed with a 444 k-grid.

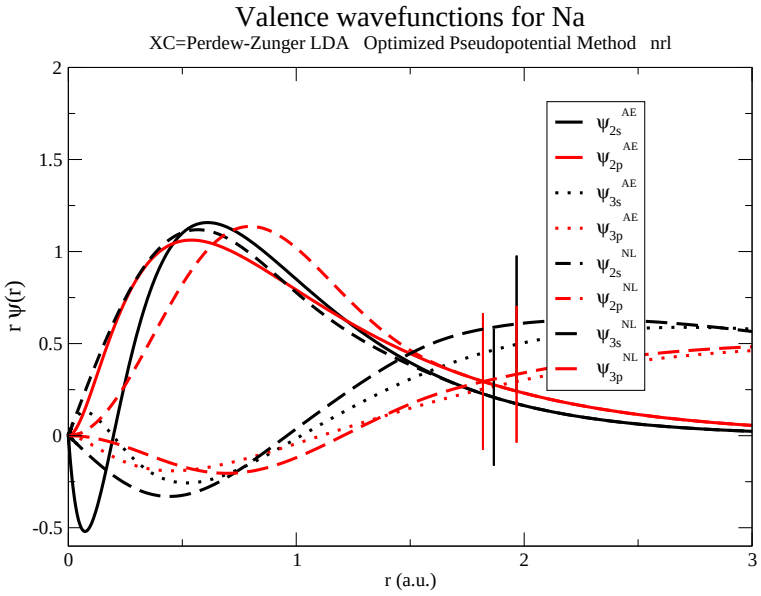

Figure 4.1: Valance wavefunctions for Na for used in thesis.

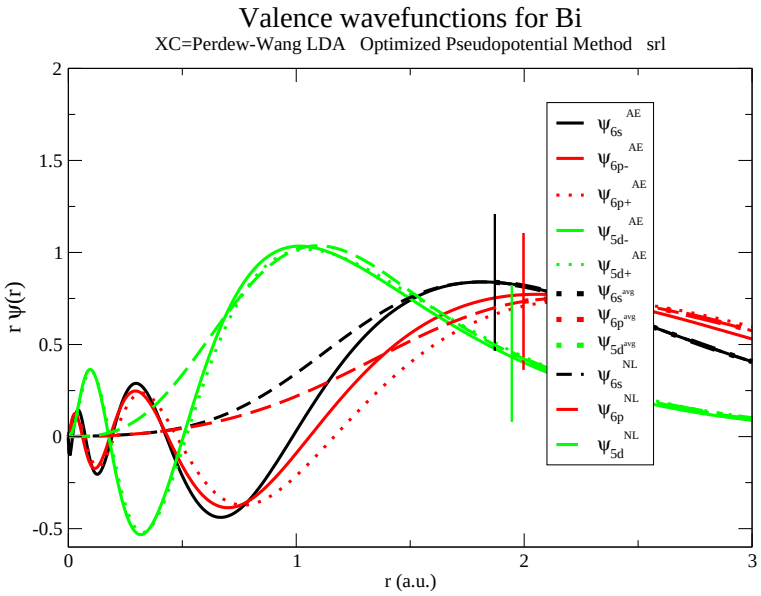

Figure 4.2: Valance wavefunctions for Bi for used in thesis.

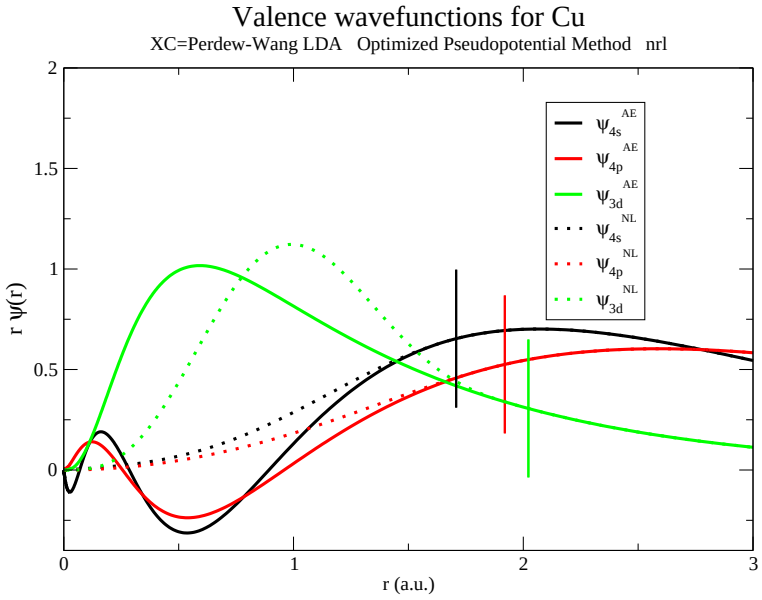

Figure 4.3: Valance wavefunctions for Cu for used in thesis.

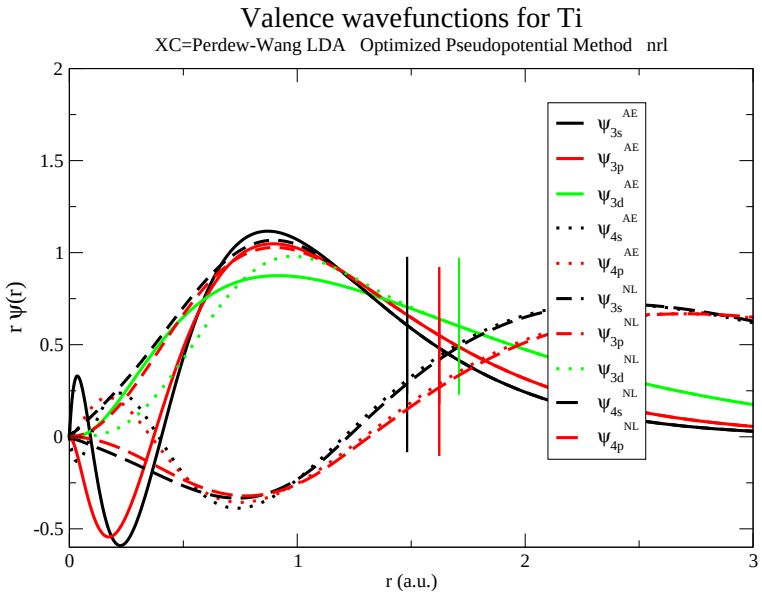

Figure 4.4: Valance wavefunctions for Ti for used in thesis.

4.2 Structural properties

The $Na_{1/2}Bi_{1/2}Cu_3Ti_4O_{12}$ crystalline structure, which is shown in Fig. 4.6, belongs to the $Pm\bar{3}$ (space group number 200) with Na, Bi, Cu, Ti and O atoms located at 1a (0,0,0), 1b (1/2,1/2,1/2), 3c (1/2,0,0), 3d (0,1/2,1/2), 8i (x_{Ti},x_{Ti},x_{Ti}), 12j

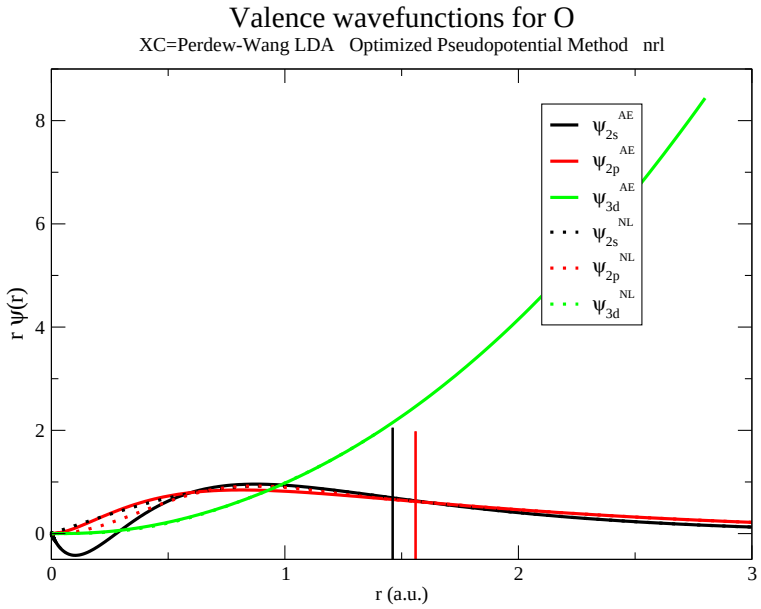

Figure 4.5: Valance wavefunctions for O for used in thesis.

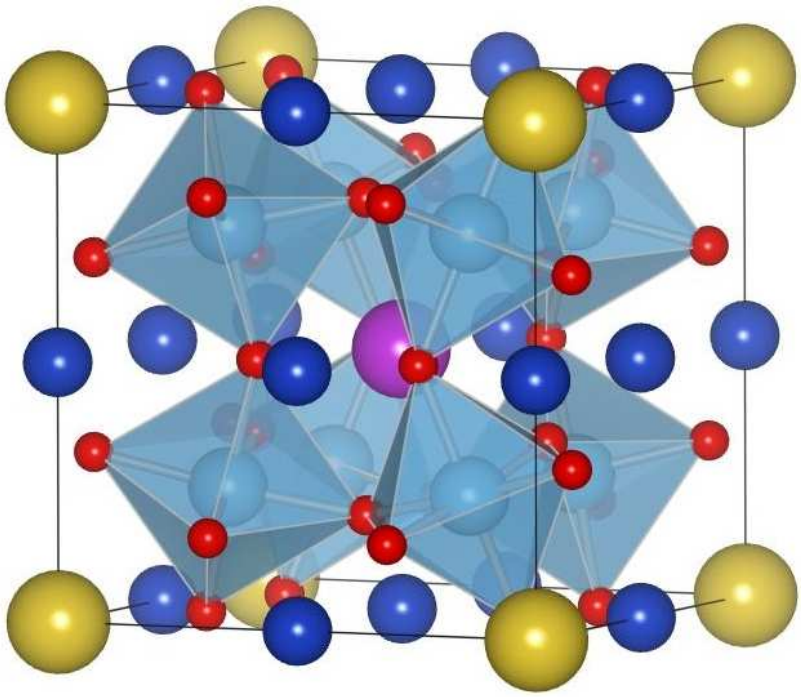

Figure 4.6: The simple cubic crystal structure of $Na_{1/2}Bi_{1/2}Cu_3Ti_4O_{12}$. The octahedra represent the TiO_6 groups with oxygen at the corners and Ti at the centers.

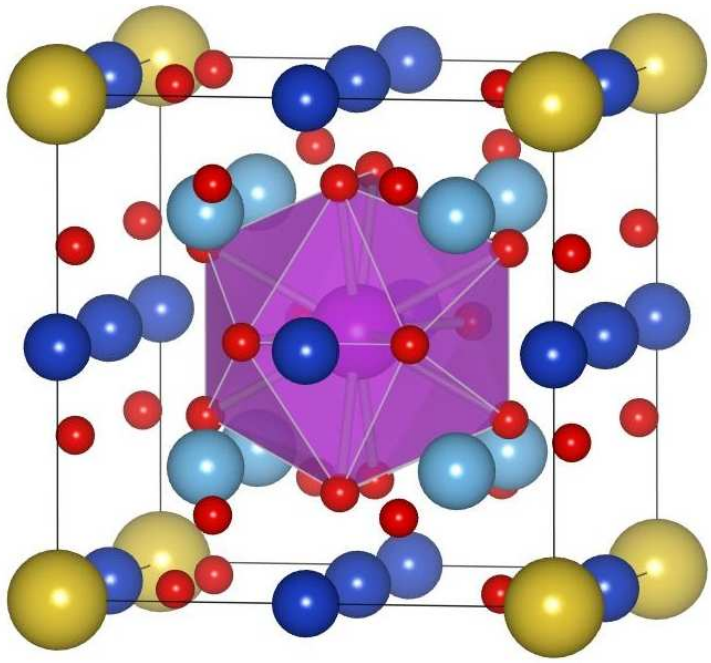

Figure 4.7: The simple cubic crystal structure of $Na_{1/2}Bi_{1/2}Cu_3Ti_4O_{12}$. The icosahedra represent the BiO_{12} groups with oxygen at the corners and Bi at the centers.

(x_{O_1}, y_{O_2}, 0) and 12k (x_{O_2}+1/2,y_{O_2}+1/2,1/2) Wyckoff positions, respectively. The primitive unit cell contains 40 atoms. Minimization of the total energy with respect to the lattice volume gives a lattice constant of 7.375 Å which is in excellent agreement with the measured value of 7.411 Å [84]. The bulk modulus (B_0) and its pressure derivative are calculated as 234 GPa and 4.46, respectively. These values can be compared to the bulk modulus of CCTO ($B_0 = 212 \pm 2$ GPa [104]) and CdCTO ($B_0 = 235 \pm 7$ GPa [105]). The equilibrium atomic positions are obtained by using BFGS algorithm, moving the atoms until the maximum force component is less than 0.5 meV/Å. The optimized x_{Ti} is found to be 0.246 which is similar to that of CCTO (x_{Ti}=0.25 [106]). The x and y parameters of the oxygen positions are found as $x_{O_1} = 0.304$ and $y_{O_1} = 0.179$. As the primitive unit cell is rather large, it contains several interesting subcells; the subsystem composed of Na and Bi atoms can be considered as a large bcc

cell with one of them occupying the center of the cell while the other is located at the vertices of the cell. The 40 atom-cell contains eight smaller bcc-like cells with center atom as Ti and vertex atoms as diagonally placed sodium and bismuth and the remaining six vertices occupied by copper atoms. As common with all the other Ti-containing perovskite-derived coasal dielectric materials, Ti cations are placed at the center of oxygen octahedra which are formed by three O_1s and three O_2s (Fig. 4.6). In each one of the octahedra, there exists two types of Ti-O bonds with lengths 1.93 (Ti-O_1) and 1.99 Å (Ti-O_2)(Ti-O bond length in CCTO is 1.96 Å [106]). The TiO_6 octahedron tilting (O-Ti-O angle=104.05^o) is also found to be similar to that in CCTO (104.64^o) [106]. Also, Cu_1O_4 and Cu_2O_4 units form planar squares with Cu_1-O_1=1.95 Å and Cu_2-O_2=1.97 Å(Fig. 4.9). Na and Bi atoms are surrounded by 12 equidistant oxygen atoms. Na-O distance (2.60 Å, Fig. 4.8) is found to be slightly longer than Bi-O distance (2.58 Å)(Fig. 4.7).

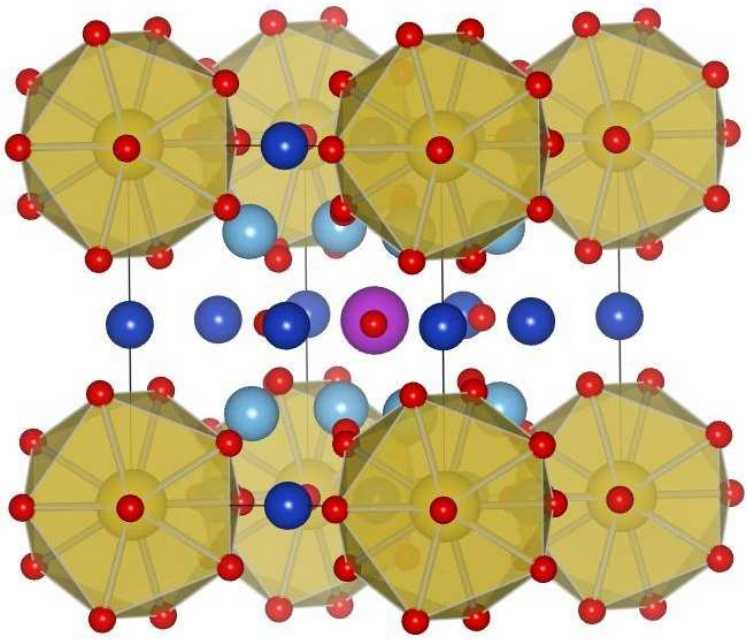

Figure 4.8: The simple cubic crystal structure of $Na_{1/2}Bi_{1/2}Cu_3Ti_4O_{12}$. The icosahedra represent the NaO_{12} groups with oxygen at the corners and Na at the centers.

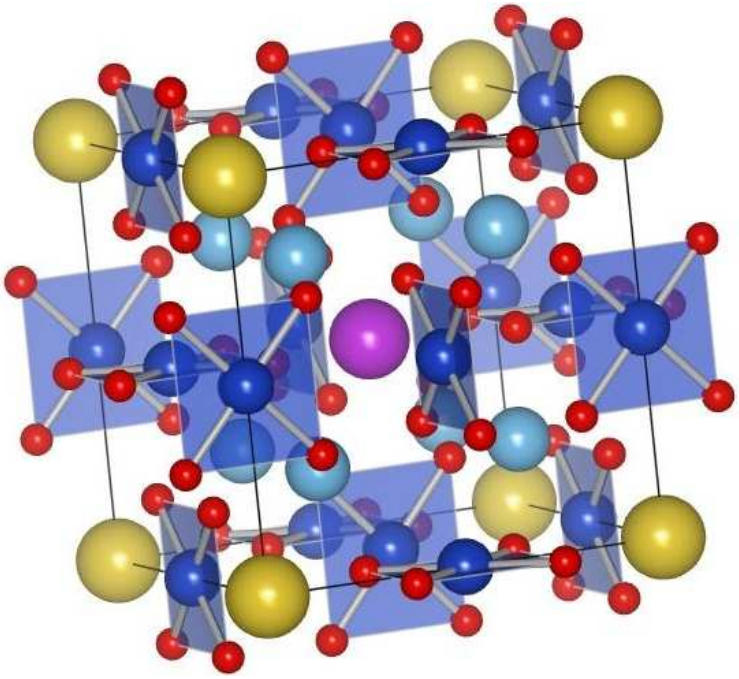

Figure 4.9: The simple cubic crystal structure of $Na_{1/2}Bi_{1/2}Cu_3Ti_4O_{12}$. The square represent the CuO_4 groups with oxygen at the corners and Cu at the centers.

4.3 Electronic structure

The electronic band structure of $Na_{1/2}Bi_{1/2}Cu_3Ti_4O_{12}$ is calculated at the theoretically determined equilibrium geometry and given in Fig. 4.10. Non spin-polarized ground state is found to be metallic with Cu 3d and oxygen 2p derived states forming the bands around the Fermi-level. Including the spin polarization decreases the total energy and leads to an antiferromagnetically ordered semiconducting state with an indirect band gap of 0.53 eV (between R and X points of the cubic Brillouin zone (Fig. 4.11)). The smallest direct band gap is 0.64 eV at the X point. The calculated band gap is, probably, too low because of well known deficiency of the local density approximation to exchange-correlation potential. The observed AFM semiconducting state is similar to the case of prototype GDC

compound CCTO which is known to exhibit an antiferromagnetic transition at ∼25 K [107, 108]. The states near the gap are mostly derived from Cu 3d and O 2p hybridization. The calculated band structure is very similar to that of CCTO reported by Ref.[95].

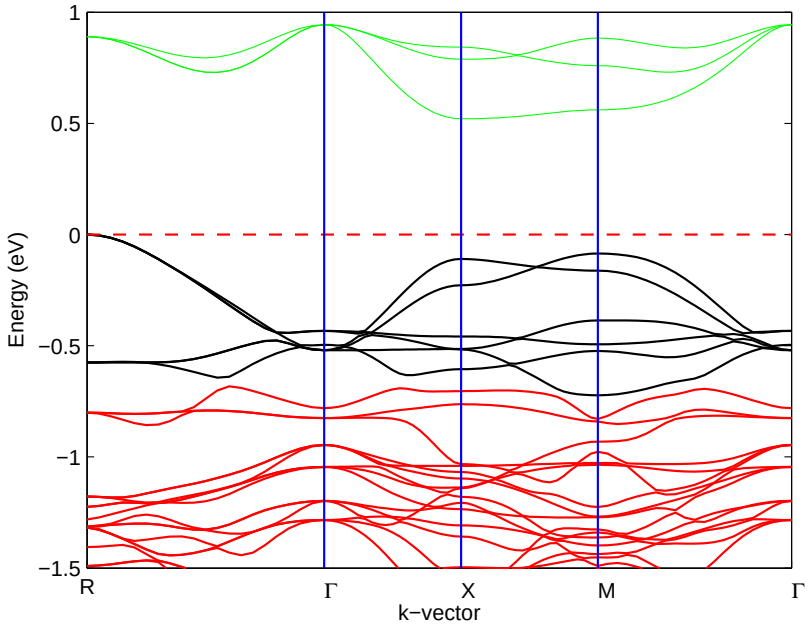

Figure 4.10: Electronic band structure of $Na_{1/2}Bi_{1/2}Cu_3Ti_4O_{12}$ along the $R-\Gamma-X-M-\Gamma$ high symmetry directions of the cubic Brillouin zone.

As a bird-eye view to a material, form of atomic charges is important quantity, both before and after bonding. And a number of way as Mulliken population analysis, Voroni analysis can be used for describing the electron density in material to the atoms that compose it. Here we report the Hirshfeld description which is an approximation to define the difference between before and after bonding charge of an atom. In this picture the total electronic charge of a bonded atom is given as $Q_i = \int \delta_i(r)dv$, here $\delta_i(r)$ is the atomic deformation density, can be define as the difference between "charge density of an bonded atom" and the "atomic density". In this case net atomic charge of a bonded atom is addition

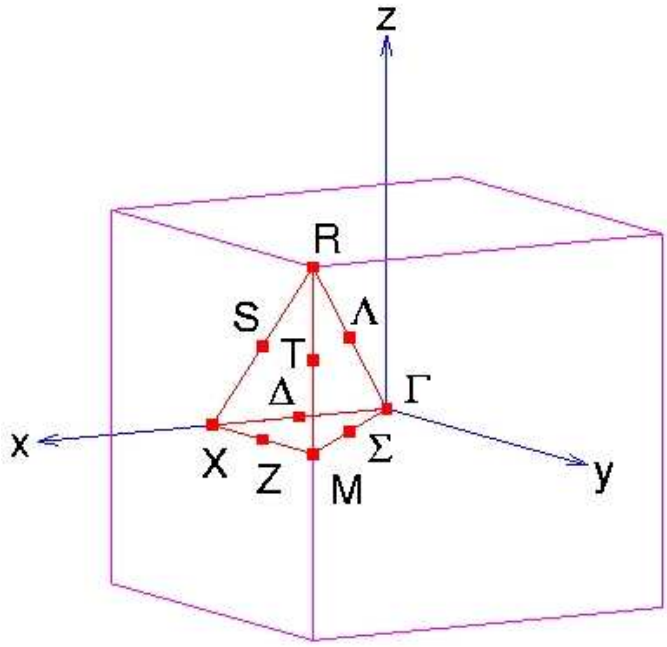

Figure 4.11: The First Brillouin zone of a simple cubic lattice, with high symmetry k points [109].

of charge deformation to charge of free atom. The calculated Hirshfeld charges (Na=0.11, Bi=0.55, Cu_1=0.44, Cu_2=0.42, Ti=0.24, O_1=-0.21 and O_2=-0.22 e) indicate that the there is net transfer of electrons to oxygen atoms from all the other constituents of the cell.

The difference between the up- and down-spin densities, which is a measure of magnetization density is displayed in Fig. 4.12 as isosurfaces for two different values of the difference. Figure 4.12 clearly reveals the Cu(3d)-O(2p) σ-antibonding nature of the magnetic density, which extend over the central cluster composed of a Cu ion and its four close oxygen neighbors at 1.95 and 1.97 Å. This cluster evidently forms a strongly spin-polarized unit with a ferromagnetic alignment of the magnetic moments on the Cu and O atoms comprising it, indicating a significant role of the oxygen atoms in the magnetic structure (Fig. 4.13). From the spin densities copper and oxygen magnetic moments are found to be be 0.52 and

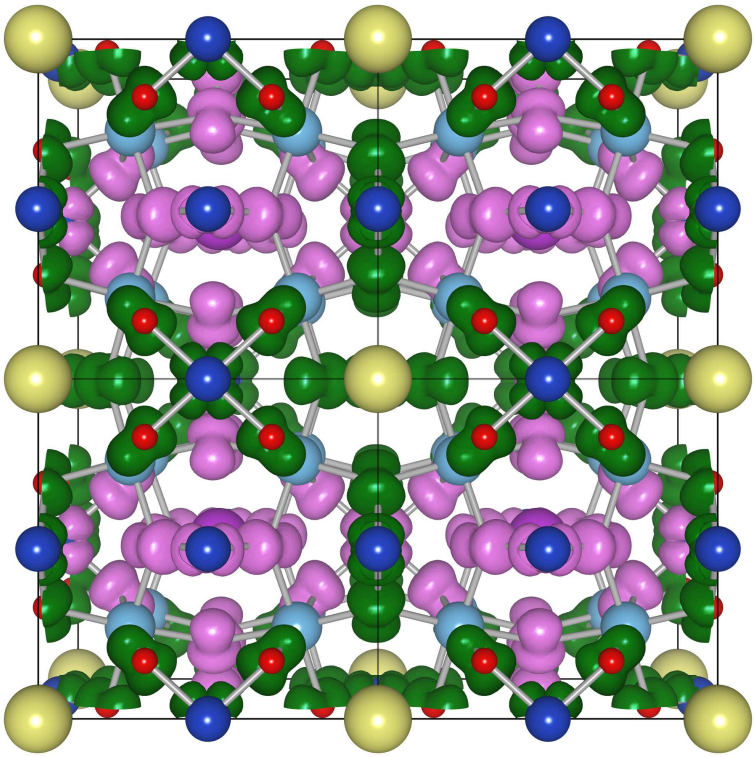

Figure 4.12: 3D isosurfaces of the difference between the up and down spin charge densities. Two different values (-0.001 (green) and 0.001 (pink)$|e|$) are displayed.

0.09 μ_B which are very close to the values reported for the CCTO [93] and total magnetic moment of CuO_4 complex is 0.88 μ_B.

4.4 Electronic dielectric tensor and Born effective charges

The Born effective charges, $Z^\star$, describe the change in the macroscopic polarization in response to the displacement of the ions and determine the splitting of the infrared active optical modes of the insulating crystals. The calculated $Z^\star$s are presented in Table 4.1 and displayed in Fig. 4.14 graphically. The charge imbalance of the cell is found to be less than 0.006 e which is an indication of the quality of convergence of the calculations. The number of nonzero compo-

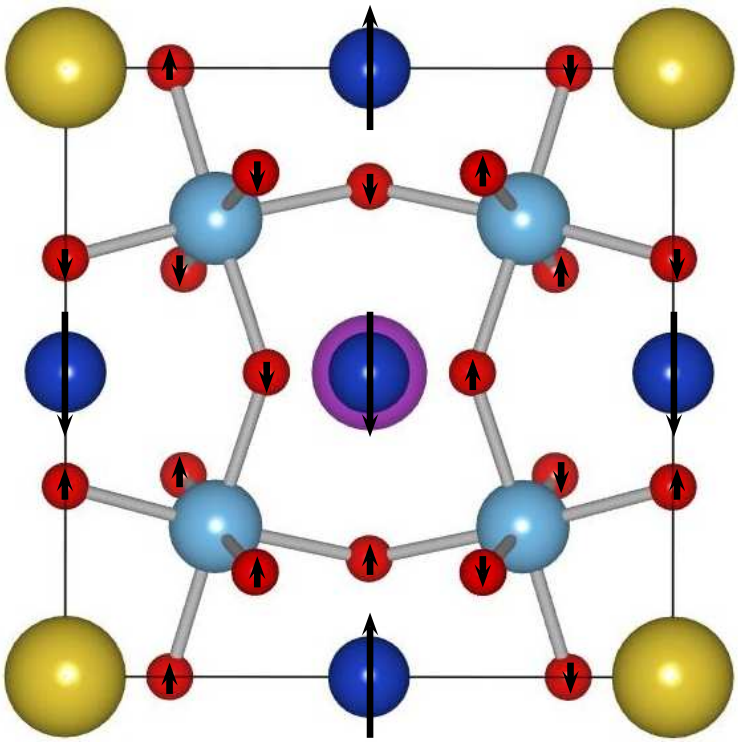

Figure 4.13: Diagrams of magnetic structure of NBCTO. Arrows represent spin up and down cases for Cu and O and meaning of bigger arrows are about five times greater magnetic moment of Cu atoms with respect to magnetic moment of O atoms.

nents of $Z^\star$ tensor for a particular atom depends on the symmetry of the site it occupies in the cell. Na and Bi are located at sites with cubic symmetry T_h and have diagonal $Z^\star$ with equal components. The site symmetry of Cu_1 and Cu_2 is D_{2h} and as a result $Z^\star(Cu)$ is diagonal with unequal components. Ti and O are located at lower symmetry sites (C_3 and C_s, respectively) and their effective charge tensors have nonzero, albeit small, off-diagonal components. The difference between $Z^\star(Cu_1)$ and $Z^\star(Cu_2)$ as well as $Z^\star(O_1)$ and $Z^\star(O_2)$ stems from the difference in local structure of CuO_4 plaques. The most important observation from Table 4.1 and Fig. 4.14 is the anomaly in Ti and O dynamical charges. The large dynamical anomalous charges (compared to the nominal ionic values of Na^{+1}, Bi^{+3}, Cu^{+2}, Ti^{+4} and O^{-2}) originate from the electronic charge reor-

ganization induced when an atom is displaced from its original position. Large values of Born effective charges have been observed in ABO_3 type perovskites and attributed to the hybridization between the occupied O 2p orbital and the unoccupied B 3d orbital [111, 110]. Our calculated Cu, Ti and O effective charges are similar to those given by He *et al.* for CCTO and CdCTO [94]. Also, the principal components of $Z^{\star}(Ti) \approx 7.20$ calculated here are comparable to the values reported as 7.16, 7.12, 7.08 and 7.06, in compounds $BaTiO_3$, $SrTiO_3$, $CaTiO_3$, and $PbTiO_3$, respectively [111]. $Z^{\star}(O)$ are also similar in NBCTO (Table 4.14) and Ti-containing perovskites [111].

Electronic part of the dielectric tensor is isotropic (as expected from the cubic T_h point group symmetry) with a value $\epsilon_{\infty} = 11.8$. There is no experimental value of ϵ_{∞} to compare but it is well known that the LDA overestimates the ϵ_{∞} because of the band-gap problem.

Table 4.1: Calculated Born effective charges of $Na_{1/2}Bi_{1/2}Cu_3Ti_4O_{12}$. The eigenvalues, λ, of the symmetric part of $Z^{\star}$ are given in brackets.

	Effective Charge Tensor	λ
$Z^{\star}_{\mathrm{Na}}$	diagonal	[1.20 1.20 1.20]
$Z^{\star}_{\mathrm{Bi}}$	diagonal	[5.37 5.37 5.37]
$Z^{\star}_{\mathrm{Cu_1}}$	diagonal	[2.11 2.21 1.15]
$Z^{\star}_{\mathrm{Cu_2}}$	diagonal	[2.45 1.70 1.19]
$Z^{\star}_{\mathrm{Ti}}$	$\begin{pmatrix} 7.21 & 0.18 & -0.04 \\ -0.04 & 7.21 & 0.18 \\ 0.18 & -0.04 & 7.21 \end{pmatrix}$	[7.13 7.13 7.34]
$Z^{\star}_{\mathrm{O_1}}$	$\begin{pmatrix} -1.86 & 0.39 & 0.00 \\ 0.60 & -1.91 & 0.00 \\ 0.00 & 0.00 & -5.58 \end{pmatrix}$	[−5.57 − 2.39 − 1.39]
$Z^{\star}_{\mathrm{O_2}}$	$\begin{pmatrix} -2.37 & -0.05 & 0.00 \\ 0.20 & -2.11 & 0.00 \\ 0.00 & 0.00 & -4.92 \end{pmatrix}$	[−4.92 − 2.39 − 2.09]

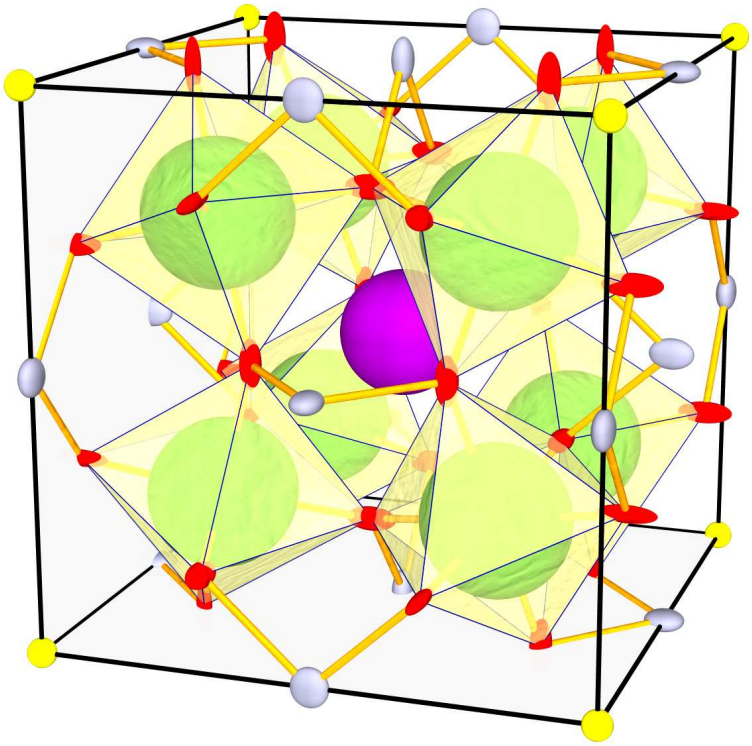

Figure 4.14: Born effective charges of $Na_{1/2}Bi_{1/2}Cu_3Ti_4O_{12}$. Here each of the atoms are taken as the unit sphere and sheared with its Born effective charge tensor.

4.5 Zone center phonon frequencies and static dielectric constant

The primitive unit cell contains 40 atoms which leads to a total of 120 phonon modes. The symmetry of modes and the number of raman and IR active phonon modes of a structure can be calculated with group theory. For all these information, one needs only symmetry of the crystal. Best of our knowledge, there is no group theoretical analysis of NBCTO in literature, therefore brief analysis was performed in this work. At the beginning, we know Wyckoff positions of five elements of unitcell which we were discussed before. Then irreducible presentations for all sites must be determined [112] and given in Table 4.2. And phonon modes

can be decomposed into the following sum of irreducible representations:

$$\Gamma = 5A_g \oplus 5E_g \oplus 11T_g \oplus 3A_u \oplus 3E_u \oplus 21T_u$$

Then, one can subtract the acoustic modes to determine the normal modes of vibrations. The meaning of normal mode is all atoms vibrate at same frequency in the corresponding mode and all atoms pass their equilibrium positions at the same time. Acoustic phonons can be described using translation vectors. The representation of the translations x,y and z can be obtained inspection by the character Table 4.3. x, y and z translations correspond the triply degenerate acoustic mode at T_u symmetry. After that, character table can be tell us about raman, IR active and silent modes. A mode will be Raman active if the normal mode belongs to the same representations as quadratic terms of Cartesian coordinates (x^2, y^2, z^2), their sums and differences (i.e. x^2-y^2, etc.) or products of Cartesian coordinates (i.e. xy, yz, etc.) [113]. A mode will be infrared active if the normal mode belongs to the same representation as the translations x, y, z. If there are no coordinates belonging to a representation, the related mode is silent.

Table 4.2: Irreducible representations of each position

Wyckoff pos.	Representations
12k	$5T_u \oplus 1A_u \oplus 2A_g \oplus 2E_g \oplus 1E_u \oplus 4T_g$
12j	$5T_u \oplus 1A_u \oplus 2A_g \oplus 2E_g \oplus 1E_u \oplus 4T_g$
8i	$3T_u \oplus 1A_u \oplus 1A_g \oplus 1E_g \oplus 1E_u \oplus 3T_g$
3d	$3T_u$
3c	$3T_u$
1b	$1T_u$
1a	$1T_u$

Among these phonon modes, only T_u modes are IR-active, A_g, E_g and T_g modes are Raman-active. A_u and E_u modes are optically silent.

We will present the properties of phonons in two groups based on the activities

Table 4.3: Character table of point group T_h.

T_h	E	$4C_3$	$4C_3^2$	$3C_2$	i	$4S_6^5$	$4S_6$	$3\sigma_h$	functions
A_g	1	1	1	1	1	1	1	1	$(x^2+y^2+z^2)$
A_u	1	1	1	1	−1	−1	−1	−1	
E_g	1	ε	ε^*	1	1	ε	ε^*	1	$(2z^2-x^2-y^2, x^2-y^2)$
	1	ε^*	ε	1	1	ε^*	ε	1	
E_u	1	ε	ε^*	1	−1	$-\varepsilon$	$-\varepsilon^*$	−1	
	1	ε^*	ε	1	−1	$-\varepsilon^*$	$-\varepsilon$	−1	
T_u	3	0	0	−1	−3	0	0	1	(x,y,z)
T_g	3	0	0	−1	3	0	0	−1	$(xz,yz,xy),(R_x,R_y,R_z)$

$\varepsilon = exp(\frac{2\pi i}{3})$

Table 4.4: TO frequencies (in cm^{-1}), mode effective charges (in $|e|$) and the mode contribution to the static dielectric constant of IR-active zone center phonons of $Na_{1/2}Bi_{1/2}Cu_3Ti_4O_{12}$.

ω_i	Z_i^*	$\Delta\epsilon_i$	ω_i	Z_i^*	$\Delta\epsilon_i$
50	9.59	63.78	299	1.86	0.28
108	10.57	25.41	335	1.98	0.32
126	3.72	1.81	381	7.45	1.36
142	9.51	15.05	406	12.41	3.37
146	3.95	2.50	436	9.25	2.55
177	5.81	4.60	492	4.62	0.36
184	4.63	2.33	496	1.96	0.10
206	1.61	0.21	533	0.53	0.00
236	11.14	13.52	540	2.63	0.17
268	1.98	0.37	682	2.94	0.14

of the modes. The first group is comprised of 21 T_u modes which are IR-active. IR-active modes determine the lattice susceptibility contribution to static dielectric constant and it is known that for most of the insulating perovskites [114] and the CCTO [93] the lattice contribution to ϵ_0 is much higher compared to the electronic one. One of the triply degenerate T_u symmetry modes forms the acoustic branch with zero frequency(Fig. 4.15). Frequency, mode effective charge and oscillator

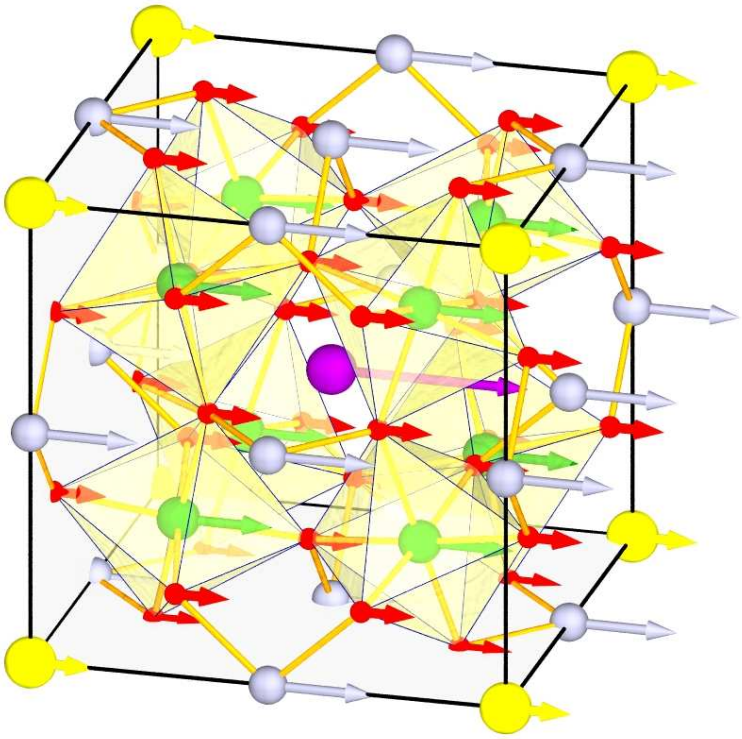

Figure 4.15: Eigendisplacement patterns of zero frequency acoustic T_u mode.

strength of the remaining 20 T_u modes are presented in Table 4.4. Since, to the best of our knowledge, there is no experimental data on phonons of NBCTO, we will compare the calculated quantities with experimental and computational data of CCTO and CdCTO. The most important finding here is the existence of a very low frequency polar mode at 50 cm^{-1} which has a large mode effective charge. The eigendisplacement of this low frequency T_u mode is displayed graphically in Fig. 4.22 and involves the anti-parallel motion of Na and Bi as a group against the Cu and O atoms. The displacement pattern of Ti atoms is a breathing type motion with much smaller amplitude compared to the displacement of the

other atoms. The low frequency T_u mode was found to be important in possible explanation of the relatively high low-temperature intrinsic dielectric constant of CCTO. Homes *et al.* [10] have found that its frequency decreases while the oscillator strength of it increases with an f-sum rule violation. The frequency of this mode is found at 125 and 72 cm^{-1} for CCTO and CdCTO by He *et al.* and ω =50 cm^{-1} calculated here seem to indicate that it is proportional to inverse square root of the mass of Ca, Cd and Bi in the three compounds. The remaining T_u mode frequencies range from 108 to 682 cm^{-1} (The highest frequency T_u mode (682 cm^{-1}) displayed in Fig. 4.17 mostly involves motion of O atoms at the bottom of the O octahedrons and almost all other atoms at rest).

The static dielectric tensor of a non-polar material can be written as the sum of the electronic dielectric permitivitiy tensor ϵ_∞ and a sum of contributions $\Delta\epsilon_i$ from each of the zone-center polar mode i :

$$\epsilon^0_{\alpha\beta} = \epsilon^\infty_{\alpha\beta} + \sum \Delta\epsilon_{i,\alpha\beta}$$

where $\Delta\epsilon_i$ given by

$$\Delta\epsilon_{i,\alpha\beta} = \frac{4\pi e^2}{M_0 V}\frac{Z^\star_{i\alpha} Z^\star_{i\beta}}{\omega_i^2}$$

here, V is the volume of the primitive unit cell and M_0 is a reference mass taken as 1 amu. The lattice contribution to the static dielectric constant of the modes given in Table 4.4 is around 138 (the highest contributions being from the modes at 50 ($\Delta\epsilon_i = 63.78$), 108 ($\Delta\epsilon_i = 25.41$), 142 ($\Delta\epsilon_i = 15.05$) and 236 ($\Delta\epsilon_i = 13.52$) cm^{-1}). Although the mode at 406 cm^{-1} has the largest mode effective charge,

its contribution to dielectric constant is low because the contribution is inversely proportional to the square of the mode frequency. The low frequency polar modes with high mode effective charges might explain the high intrinsic dielectric constant of 235 reported by Ferrarelli *et al.* [84] for NBCTO. The relatively low values of the minimum optical frequencies in NBCTO is partly related to the high mass of bismuth. Modes with frequencies larger than 200 cm^{-1} involve, mostly, the motion of Cu and O atoms while all the atoms partake in the lower frequency modes. Comparing our calculated high frequency T_u modes with those of CCTO and CdCTO [94], one can see that the effect of A cation is minimal in determination of frequencies of these modes; this finding is expected because the mode patterns of these modes involve motion of Cu, Ti and O atoms only. It seems relatively safe to argue that the high intrinsic static dielectric constant observed in GDCs is related to the anomalous Born effective charges which is common for Ti-O octahedral structure and low frequency polar phonon mode whose frequency inversely scales with the square root of the cation mass.

An interesting observation on the effect of Coulomb interaction on the polar modes of perovskite ferroelectrics is the giant LO-TO splitting of the IR-active polar modes [111]. Meaning of LO-TO splitting is the shift of in frequency between longitudinal optical phonons and transverse optical phonons (other means that is removal of degeneracy between LO and TO frequencies) at the Brillouin zone center, due to the long range forces between atoms as macroscopic electric field (Coulomb interaction) associated with long wave longitudinal optical phonons. In polar crystals, the non-analyticity of dynamical matrices in long wave limit produce LO-TO splitting of polar modes. In this limit, one can write dynamical matrices as:

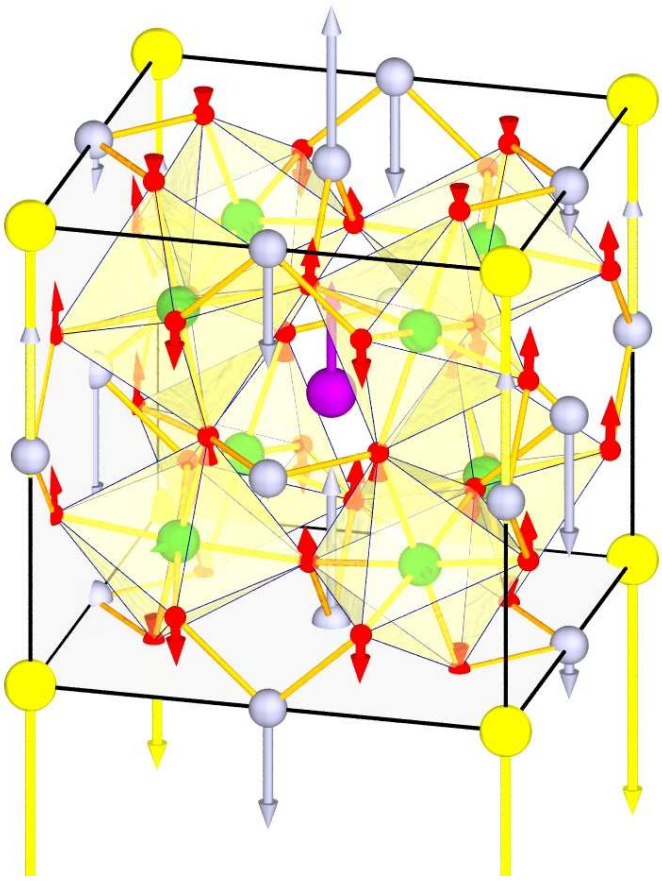

Figure 4.16: Eigendisplacement patterns of the lowest frequency A_u mode.

$$\widetilde{C}_{\kappa\alpha,\kappa'\beta}(\mathbf{q}\to 0) = \widetilde{C}^{AN}_{\kappa\alpha,\kappa'\beta}(\mathbf{q}=0) + \widetilde{C}^{NA}_{\kappa\alpha,\kappa'\beta}(\mathbf{q}\to 0) \tag{4.1}$$

where analytic part given by $\widetilde{C}^{AN}_{\kappa\alpha,\kappa'\beta}$ is the matrix obtained from the a zone-center phonon, calculated at zero macroscopic electric field.

The non-analytic part:

$$\widetilde{C}^{NA}_{\kappa\alpha,\kappa'\beta}(q\to 0) = \frac{4\pi}{\Omega}e^2\frac{\sum_\gamma Z^{\star\gamma}_{\kappa\alpha}q_\gamma \sum_\nu Z^{\star\nu}_{\kappa'\beta}q_\nu}{\sum_{\gamma,\nu} q_\gamma \widetilde{\epsilon^{\gamma\nu}_\infty} q_\nu} = \frac{4\pi}{\Omega}e^2\frac{(\mathbf{q}.\mathbf{Z}^\star_\kappa)_\alpha(\mathbf{q}.\mathbf{Z}^\star_{\kappa'})_\beta}{\mathbf{q}.\epsilon_\infty.\mathbf{q}} \tag{4.2}$$

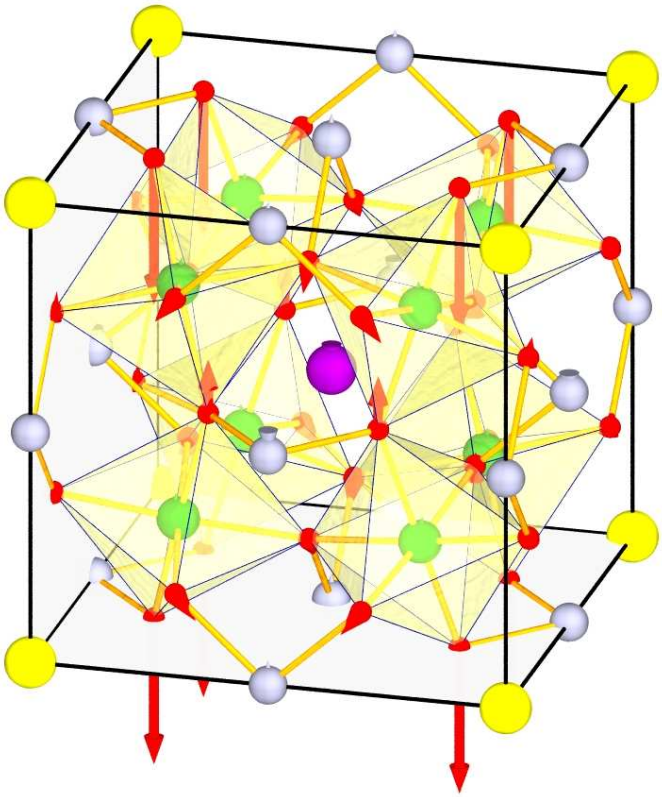

Figure 4.17: Eigendisplacement patterns of the highest frequency T_u mode.

As seen in Equation 4.2 we need only information of macroscopic dielectric constant ϵ_∞ and Born effective charges Z* (all quantities directly accessible within DFPT) of system to calculate the non-analytical part. In this point direction dependencies of ϵ_∞s and Z*s, effect to solution of $\widetilde{C}^{NA}_{\kappa\alpha,\kappa'\beta}$ and so that we get different phonon frequencies at longitudinal and transverse branches. And analytical term can be calculated when ignoring any macroscopic polarization associated with phonons [3].

An investigation of the overlap matrix of mass matrix $M_{mn} = M_m\delta_{mn}$ between the LO and TO mode eigenvectors as $c_{ij} = \langle\xi_i^{\mathrm{TO}}|M|\xi_j^{\mathrm{LO}}\rangle$. The overlap matrix for

NBCTO is given in figure 4.18. Although some of the TO modes (at 185, 299 and 540 cm^{-1}) have appreciable overlap with more than one LO mode, there is no giant-splitting in any of the modes. The largest LO-TO splitting is found for the TO mode at 533 cm^{-1} which has corresponding LO frequency of 613 cm^{-1}.

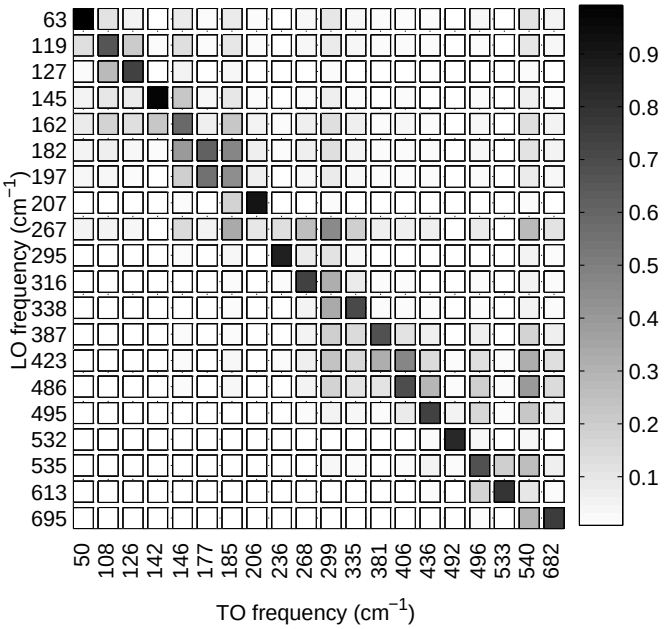

Figure 4.18: LO-TO overlaps of the IR-active modes.

Table 4.5: Non-polar phonon mode frequencies (cm^{-1}).

Mode symmetry											
A_g	295	409	464	497	517						
E_g	272	308	378	533	557						
T_g	105	125	180	267	295	388	430	434	478	518	719
A_u	145	415	753								
E_u	103	436	514								

The frequencies of Raman-active and silent modes are given in Table 4.5. One of the silent mode which is lowest frequency A_u mode, displayed in Fig. 4.16. Contrary with the almost all other modes, this mode involves motion of all atoms

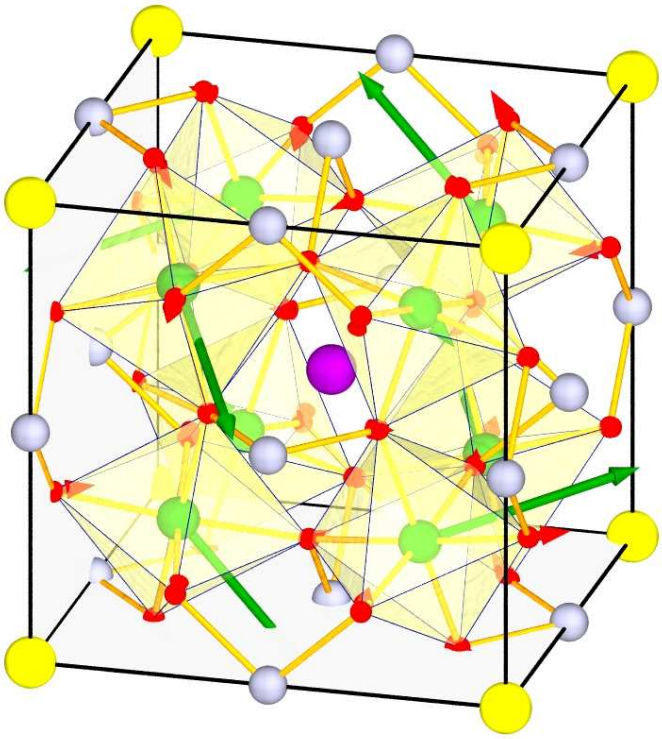

Figure 4.19: Eigendisplacement patterns of the lowest frequency T_g mode.

and heavy Bi atoms and Cu atoms has relatively high displacement. The Raman-active modes can be broadly divided into four groups based on the magnitude of the vibration frequency as follows: a low frequency group of modes with T_g symmetry and $\nu \approx 105$ (for lowest frequency T_g mode, one can say Ti atoms located middle of the O octahedrons has big displacement and O atoms has relatively low displacement (Fig. 4.19)) and 180 cm^{-1}, a group of modes in the $\nu \approx 267$ and 308 cm^{-1} range (one from each one of the symmetries), a total of 11 modes in the 378-557 cm^{-1} range and finally the highest frequency T_g mode at 719 cm^{-1} which is comparable to 739 cm^{-1} reported for the highest

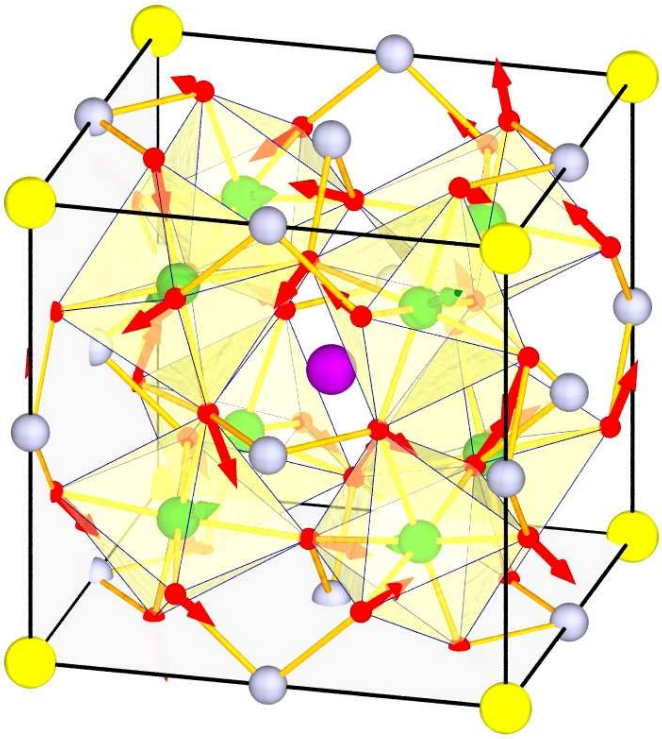

Figure 4.20: Eigendisplacement patterns of the lowest frequency E_g mode.

frequency T_g mode for CCTO [93]. Modes of T_g symmetry mainly consist of collective TiO_6 octahedral rotational or octahedral breathing type displacements. The calculated highest frequency A_g, E_g and T_g modes at 517, 557 and 719 cm^{-1}, respectively, are similar to those reported for CCTO at 519, 568 and 729 cm^{-1}. The eigendisplacement patterns of the highest frequency A_g, E_g and T_g modes are displayed in Fig. 4.23, Fig. 4.24 and Fig. 4.25 respectively. All of the Raman-active modes shown in Figures 4.23, 4.24, 4.25 and 4.21 involve, mostly, various breathing type motion of oxygen octahedra. The displacement of Ti atoms are of clockwise or anti-clockwise rotation type with much smaller amplitude compared

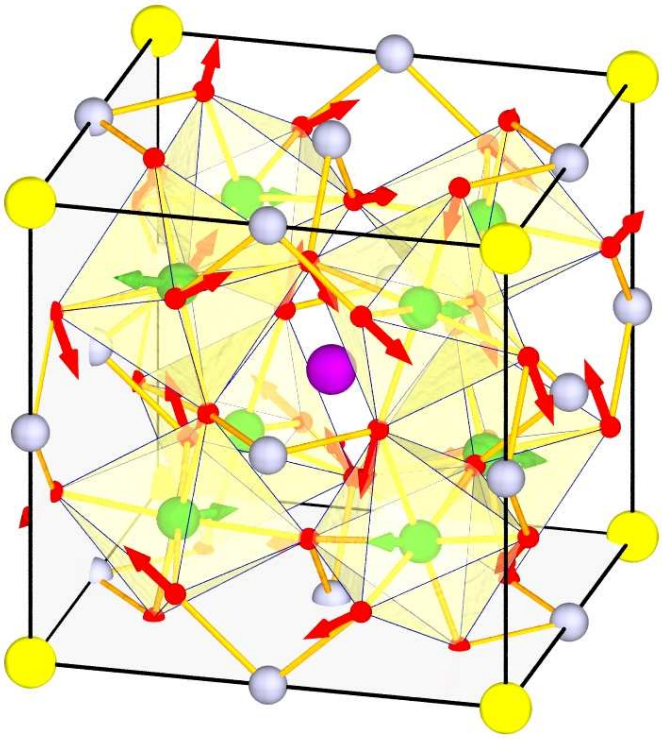

Figure 4.21: Eigendisplacement patterns of the lowest frequency A_g mode.

to those of oxygens. Same thing can be seen in Fig. 4.20 for the lowest frequency E_g mode as an example. In addition one can say for highest frequency mode (753 cm^{-1}, A_u mode), this mode looks like Raman-active modes mentioned before and mostly involves motion of O atoms at the corner of the O octahedra, but in this mode Ti atoms nearly at rest (Fig. 4.26). And we have given eigendisplacements of all atoms in unitcell for each phonon modes proportional to the square root of mass of considered atom ($\sqrt{m_i}$) in Figure 4.27.

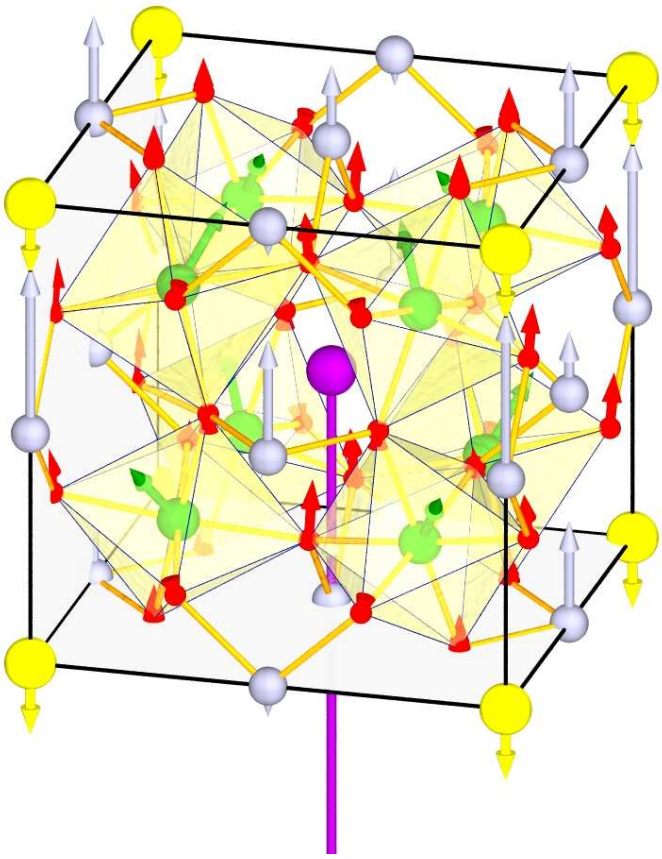

Figure 4.22: Eigendisplacement patterns of the lowest frequency T_u mode.

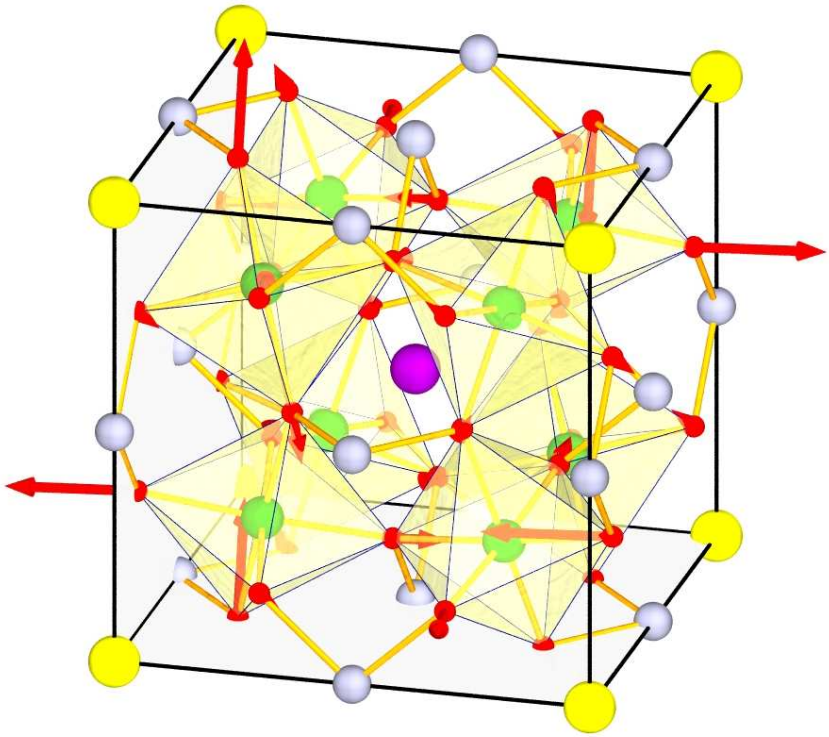

Figure 4.23: Eigendisplacement patterns of the highest frequency A_g mode.

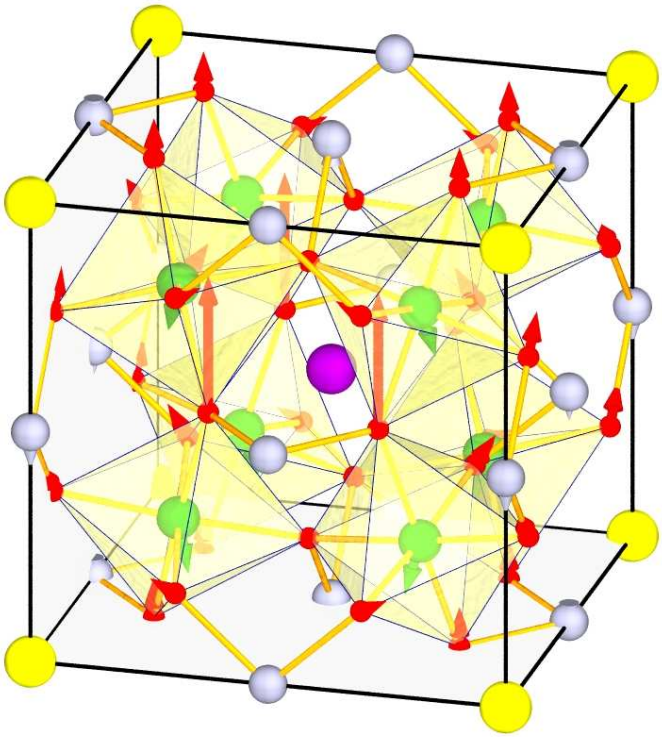

Figure 4.24: Eigendisplacement patterns of the highest frequency E_g mode.

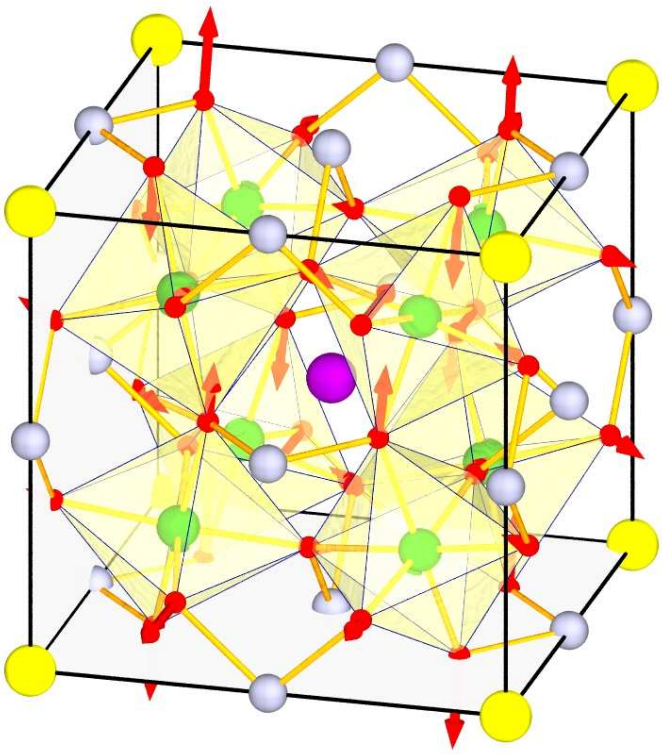

Figure 4.25: Eigendisplacement patterns of the highest frequency T_g mode.

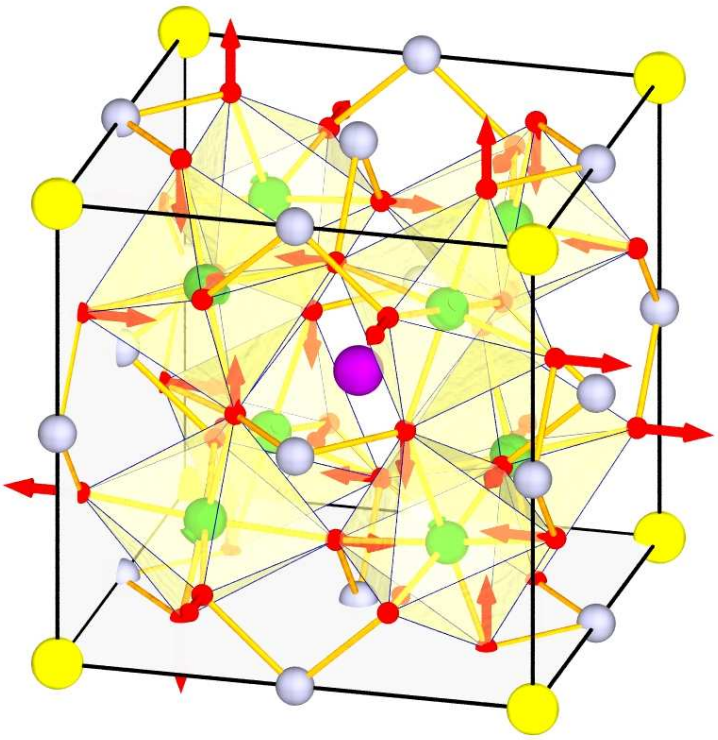

Figure 4.26: Eigendisplacement patterns of the highest frequency mode.

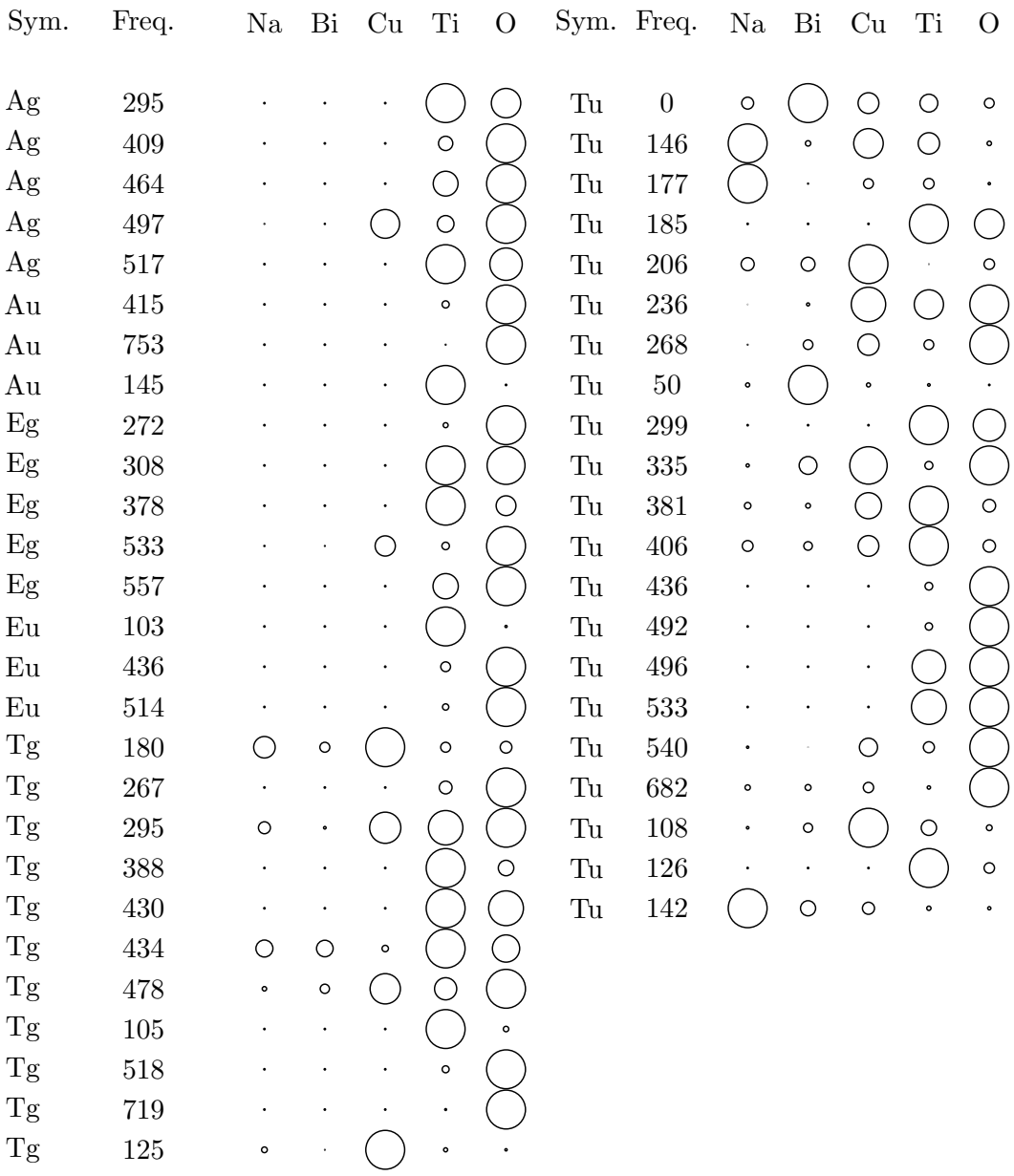

Figure 4.27: Eigendisplacement patterns of the vibrational modes. Radius of bubbles proportional to square root of mass of atoms and its displacement. Mode frequencies (Freq.) in cm^{-1}.

CHAPTER 5

CONCLUSION

In this thesis we have studied pressure-dependent lattice dynamical properties of ternary chalcopyrite semiconductors $CuAlS_2$ and $CuGaSe_2$ and the structural, electronic and lattice dynamical properties of the high-dielectric compound $Na_{1/2}Bi_{1/2}Cu_3Ti_4O_{12}$ within density functional and density functional perturbation theory framework with norm-conserving pseudopotentials a plane wave basis set.

At the first step of this work we have investigated the pressure dependent lattice dynamical properties, such as Born effective charge tensor, Brillouin zone center phonon frequencies, and static and high frequency dielectric tensors of ternary semiconductor $CuAlS_2$ and $CuGaSe_2$ within the density functional perturbation theory framework.

We have found that the pressure dependence of these quantities show similar trends with binary tetrahedrally coordinated compounds. The pressure derivatives of the components of elastic stiffness tensor of $CuGaSe_2$ were found to be similar in magnitude and sign to those of the isoelectronic binary analog compound ZnSe; while at $P = 0$ all of them are positive, at elevated pressures the pressure derivative of C_{44} and C_{66} become negative.

The pressure dependence of lattice dynamical properties such as Born effective charge tensor, Brillouin zone center phonon frequencies, and static and high frequency dielectric tensors were, also, found to show similar trends with binary tetrahedrally coordinated compounds. Formation of $Z^{\star}$s determined by location

of atoms. Cations located at $4a$ and $4b$ Wyckoff positions and it has ≈12.5% for Cu and ≈-9.2% for Ga anisotropies for $CuGaSe_2$, these anisotropies are higher than those seen in $CuAlS_2$ (4% for Cu and 2% for Al). Se and S atoms located at lower symmetry sites ($8d$ positions) and as a result their effective charge tensors have nonequivalent diagonal components as well as sizable off-diagonal components. Our calculations show the dynamical charges show no anomalous behavior as expected for some mentioned systems. Under hydrostatic pressure, the dynamical effective charges decrease. Our calculated electronic (ϵ_∞) and static (ϵ_0) dielectric tensors have two independent components $\epsilon^{\parallel}$ and $\epsilon^{\perp}$ along and perpendicular to the c axis, respectively. All of the components decrease under pressure; the volume dependence of static (high-frequency) components is slightly (highly) nonlinear, especially at higher pressures, which is similar to what has been found for the most tetrahedrally coordinated semiconductors.

The zone-center modes originating from the modes with negative Grüneisen parameter in zinc-blende materials, have negative Grüneisen parameters and the ordering of $\gamma_{TO} > \gamma_{LO}$ is respected for the zone-center chalcopyrite modes that originate from the zone-center polar mode of zinc-blende structure.

An overall finding from the pressure dependence of the response quantities considered in this study is the general similarity of the behavior in the chalcopyrite ternary compound and the zinc-blende binary compounds. This finding is partly expected because the local bonding and structural modification from the zinc-blende to chalcopyrite transformation is not very high as an example can be seen from the u (=0.27 instead of 0.25) and η (=1.97 instead of 2) values for $CuGaSe_2$.

Second part of these dissertation, we have investigated the structural, electronic and lattice dynamical properties of the high-dielectric compound NBCTO with in the local spin density approximation. The main features of the struc-

ture are found to be tilted TiO_6 octahedra, planar square CuO_4 units and 12-coordinated NaO_{12} and BiO_{12} icosahedra. The compound is found to be antiferromagnetic insulator with an indirect band gap of 0.53 eV. The electronic structure near the valance band maximum and conduction band minimum is found to be mainly originating from the hybridization of Copper 3d and Oxygen 2p states, as is common in many compounds that contain CuO_4 planar structures. The magnetic moments of Cu and O atoms are found to be 0.52 μ_B and 0.09 μ_B, respectively. These values are similar to those reported for the other GDCs.

The dynamical Born effective charges were found to be close to nominal values of Na(nominal +1 versus $Z^\star = 1.20$), Bi(nominal +3 versus $Z^\star = 5.47$) and Cu(nominal +2 versus $Z^\star_{av} = 1.90$) atoms while the $Z^\star$ of Ti and O atoms are anomalous, with components as large as 7.21 for Ti and -5.58 for the oxygen. The lattice contribution to the static dielectric constant is calculated to be ≈ 138 which is mostly due to the four IR-active modes with frequency less than 236 cm^{-1}. The highest contribution to the static dielectric constant from mode at 50 cm^{-1}, but the mode at 406 cm^{-1} has largest effective charge , its contribution is low because of these values proportional to square root of the mode frequency. The high mass of bismuth nearly cause of low values of optical frequencies in NBCTO. And if we compare our results with results of CCTO and CdCTO, we can say that A cation has relatively minumum effect on high frequencies T_u modes. And the high intrinsic static dielectric constant in GDCs is related to the anomalous Born effective charges which is common for Ti-O octahedral structure and low frequency polar phonon mode whose frequency inversely scales with the square root of the cation mass.

Well known different observation on the effect of Coulomb interaction on the polar modes of perovskite ferroelectrics is giant LO-TO splitting of the IR-active

polar modes. Although some of the TO modes (at 185, 299 and 540 cm^{-1}) have appreciable overlap with more than one LO mode, there is no giant-splitting in any of the modes. The largest LO-TO splitting is found for the TO mode at 533 cm^{-1} which has corresponding LO frequency of 613 cm^{-1}.

The total static dielectric constant, $\epsilon_0 \approx 150$ is much smaller than the experimentally reported value of 3400 above 100 K, but close to the low temperature value of 235. This finding suggests that the origin of the coastal ϵ reported for $Na_{1/2}Bi_{1/2}Cu_3Ti_4O_{12}$ is, also, extrinsic.

So we found generally well agreement between our calculations and some available data for mentioned two study.

REFERENCES

[1] P. Hohenberg and W. Kohn, *Inhomogeneous Electron Gas*, Phys. Rev. **136**, B864 (1964).

[2] W. Kohn and L. J. Sham, *Self-Consistent Equations Including Exchange and Correlation Effects*, Phys. Rev. **140**, A1133 (1965).

[3] Stefano Baroni, Stefano de Gironcoli, Andrea Dal Corso, and Paolo Giannozzi, *Phonons and Related Crystal Properties from Density-Functional Perturbation Theory*, Rev. Mod. Phys. **73**, 515 (2001).

[4] K. Kunc and R. M. Martin, *Ab initio Calculation of Phonon Spectra*, p.**65**, Plenum, New York (1983).

[5] A. Mujica, A. Rubio, A. Munoz, and R. J. Needs, *High-pressure Phases of group−IV, III−V, and II−VI Compounds*, Rev. Mod. Phys. **75**, 863 (2003).

[6] H. Tanino, T. Maeda, H. Fujikake, H. Nakanishi, S. Endo, and T. Irie, *Raman Spectra of* $CuInSe_2$, Phys. Rev. B **45**, 13323 (1992).

[7] G. D. Holah, J. S. Webb, and H. Montgomery, *Lattice−Dynamics of* $AgGaS_2$, J. Phys. C: Sol. State Phys. **7**, 3875 (1974).

[8] A. M. Mintairov, N. A. Sadchikov, T. Sauncy, M. Holtz, G. A. Seryogin, S. A. Nikishin, and H. Temkin, *Vibrational Raman and Infrared Studies of Ordering in Epitaxial* $ZnSnP_2$, Phys. Rev. B **59**, 15197 (1999).

[9] R. Trommer, E. Anastassakis, and M. Cardona, edited by M. Balkanski, R. C. C. Leite and S. P. S. Porto, *in Light Scattering in Solids*, p.**396** Wiley, New York, (1976).

[10] C. C. Homes, T. Vogt, S. M. Shapiro, S. Wakimoto, and A. P. Ramirez, *Optical Response of High Dielectric Constant Perovskite-Related Oxide*, Science **293**, 673 (2001).

[11] M.A. Subramanian and A.W. Sleight, $ACu_3Ti_4O_{12}$ *and* $ACu_3Ru_4O_{12}$ *Perovskites: High Dielectric Constants and Valence Degeneracy*, Solid State Sci. **4**, 347 (2002).

[12] J. Ihm, A. Zunger, and M. L. Cohen, *Momentum-Space Formalism for the Total Energy of Solids*, J. Phys. C **12**, 4409 (1979).

[13] Neil W. Ascroft and N. David Mermin, *Solid State Physics*, Chap. **8**, Saunders College Publishing, (1975).

[14] William H. Press, Saul A. Teukolsky, William T. Vetterling, and Brian P. Flannery, *Numerical Recipes in C*, Cambridge University Press (1988).

[15] M. C. Payne, M. P. Teter, D. C. Allan, T. A. Arias, and J. D. Joannopoulos, *Iterative Minimization Techniques for Ab initio Total-Energy Calculations: Molecular Dynamics and Conjugate Gradients*, Rev. Mod. Phys. **64**, 1045 (1992).

[16] A. M. Gaber, J. R. Tuttle, D. S. Albin, A. L. Tennant, and M. A. Contreras, edited by R. Noufi, *in 12th NREL Photovoltaic Program Rewiev*, AIP Conf. Proc. No. 306 p.**59** AIP, New York, (1994).

[17] R. W. Birkmire and E. Eser, *Polycrystalline Thin Film Solar Cells: Present Status and Future Potential*, Annu. Rev. Mater. Sci. **27**, 625 (1997).

[18] J. L. Shay, B. Tell, and H. M. Kasper, *Experimental Studies of Energy-Band Structure of $I-III-VI_2$ Semiconductors*, J B. Am. Phys. Soc. **17**, 349 (1972).

[19] L. Roa, J. C. Chervin, A. Chewvy, M. Davila, P. Grima, and J. Gonzalez, *Optical Absorption and Raman Scattering Measurements in $CuAlSe_2$ at High Pressure*, phys. stat. sol. (b) **198**, 99 (1996).

[20] M. A. Contreras, B. Egaas, K. Ramanathan, J. Hiltner, A. Swartzlander, F. Hasoon, and R. Noufi, *Progress Toward 20% Efficiency in $Cu(In,Ga)Se_2$ Polycrystalline Thin-Film Solar Cells*, Prog. in Photovoltaics **7**, 311 (1999).

[21] S. Siebentritt, A. Bauknecht, A. Gerhard, U. Fiedeler, T. Kampschulte, S. Schuler,W. Harneit, S. Brehme, and J. Albert, *$CuGaSe_2$ Solar Cells Prepared by MOVPE*, Solar Energy Materials and Solar Cell **67**, 129 (2001).

[22] C. Parlak and R. Eryiğit, *Ab initio Vibrational and Dielectric Properties of the Chalcopyrite $CuInSe_2$*, Phys. Rev. B **66**, 165201 (2002).

[23] J. Lazewski, H. Neumann, K. Parlinski, G. Lippold, and B. J. Stanbery, *Lattice Dynamics of CuAu-Ordered $CuInSe_2$*, Phys. Rev. B **68**, 144108 (2003).

[24] H. Neumann, *Lattice Dynamics and Related Properties of $A^I B^{III} C_2^{IV}$ and $A^{II} B^{IV} C_2^V$ Compounds, I. Elastic Constants*, Crys. Res. Technol. **39**, 939 (2004).

[25] W. H. Koschel, V. Hohler, A. Räuber, and J. Baars, *Optical Phonons in $CuAlS_2$*, phys. stat. sol. (b) **13**, 1011 (1973).

[26] W. H. Koschel and M. Bettini, *Zone-Centered Phonons in $A^I B^{III} S_2$ Chalcopyrites*, phys. stat. sol. (b) **72**, 729 (1975).

[27] L. Roa, J. González, J. C. Chervin, and A. Chevy, *High Pressure Raman Scattering Study of $CuAlS_2$*, phys. stat. sol. (b) **211**, 429 (1999).

[28] B. H. Bairamov, A. Aydinli, I. V. Bodnar, Yu V. Rud, V. K. Nogoduyko, and V. V. Toporov, *High Power Gain for Stimulated Raman Amplification in $CuAlS_2$*, J. Appl. Phys. **80**, 5564 (1996).

[29] M. Bettini and W. B. Holzapfel, *Grüneissen Parameters of Gamma-Phonons in $CdSiP_2$, $CuAlS_2$ and $CuGaS_2$*, Sol. Stat. Commun. **16**, 27 (1975).

[30] I. V Bodnar, A. G. Karoza, and G. F. Smirnova, *Lattice Reflectivity Spectra of $CuGaS_2$-$CuGaSe_2$ Solid-Solutions*, phys. stat. sol. (b) **84**, K65 (1977).

[31] I. V Bodnar, G. F. Smirnova, T. V. Smirnova, YU. A. Aleshchenko, and L. K. Vodopyanov, *Lattice-Vibrations of $CuGaSe_2$, $CuInSe_2$ Ternary Compounds, and $CuGa_xIn_{1-x}Se_2$ Solid-Solutions*, phys. stat. sol. (b) **145**, 117 (1988).

[32] A. M. Andrish, N. N. Syrbu, M. S. Iovu, and V. E. Tezlavan, *Infrared Vibrational-Modes and Anisotropy of the Effective Ionic Charge in $CuAlSe_2$, $CuAlS_2$, and $CuGaSe_2$*, phys.stat. sol. (b) **187**, 83 (1995).

[33] N. N. Syrbu, M. Bogdanash, V. E. Tezlevan, and I. Mushcutariu, *Lattice Vibrations in $CuIn_{1-x}Ga_xSe_2$ Crystals*, Physica B **229**, 199 (1997).

[34] W. Gebicki, J. Filipowicz, and R. Bacewicz, *Raman Scattering in Novel $(CuAlSe_2)_x(2ZnSe)_{1-x}$ and $(CuGaSe_2)_x(2ZnSe)_{1-x}$ Mixed Crystals*, J. Phys.: Condens. Matter **8**, 8695 (1996).

[35] I. V Bodnar, G. F. Smirnova, A. G. Karoza, and A. P. Chernyakova, *Vibrational-Spectra of $CuGaS_2$ and $CuGaSe_2$ Compounds and $CuGaS_{2x}Se_{2(1-x)}$ Solid-Solutions*, phys. stat. sol. (b) **158**, 469 (1990).

[36] C. Rincón and F. J Rámirez, *Lattice-Vibrations of $CuInSe_2$ and $CuGaSe_2$ by Raman Microspectrometry*, J. Appl. Phys. **72**, 4321 (1992).

[37] F. J. Rámirez and C. Rincón, *Polarized Micro-Raman Spectra in $CuGaSe_2$*, Solid State Commun. **84**, 551 (1992).

[38] J. González and J. C. Chervin, *High-Pressure Behavior of Raman Modes in $CuGaSe_2$*, Jpn. J. Appl. Phys. Suppl. **32-3**, 575 (1993).

[39] K. Wakita, T. Miyazaki, Y. Kikuno, S. Takata, and N. Yamamoto, *Resonant Raman Affect on A $CuGaSe_2$ Crystal Grown by the Traveling Heater Method*, Jpn. J. Appl. Phys. **38**, 664 (1999).

[40] C. Xue, D. Papadimitriou, Y. S. Raptis, N. Esser, W. Richter, S. Siebentritt, and M. Ch. Lux-Steiner, *Compositional Dependence of Raman Scattering and Photoluminescence Emission in $Cu_xGa_ySe_2$ Thin Films*, J. Appl. Phys. **94**, 4341 (2003).

[41] I. V Bodnar, L. V. Golubev, V. G. Plotnichhenko, and E. A. Smolyaninova, *Raman-Scattering in $CuGaSe_2$*, phys. stat. sol. (b) **105**, K111 (1981).

[42] F. W. Ohrendorf and H. Haeuseler, *Lattice Dynamics of Chalcopyrite Type Compounds. Part I. Vibrational Frequencies*, Cryst. Res. Technol. **34**, 339 (1999).

[43] X. Gonze, J.-M. Beuken, R. Caracas, F. Detraux, M. Fuchs, G.-M. Rignanese, L. Sindic, M. Verstraete, G. Zerah, F. Jollet, M. Torrent, A. Roy, M. Mikami, Ph. Ghosez, J.-Y. Raty, and D. C. Allan, *The ABINIT code is a common project of the Universite´ Catholique de Louvain, Corning Incorporated, and other contributors* (www.abinit.org), Comput. Mater. Sci. **25**, 478 (2002).

[44] S. Godecker, *Fast Radix 2, 3, 4, and 5 Kernels for Fast Fourier Transformations on Computers with Overlapping Multiply-Add Instructions*, SIAM(Soc. Ind. Appl. Math.) J. Sci. Stat. Comput. **18**, 1605 (1997).

[45] X. Gonze, *Towards A Potential-Based Conjugate Gradient Algorithm for Order-N Self-Consistent Total Energy Calculations*, Phys. Rev. B **54**, 4383 (1996).

[46] J. P. Perdew and Y. Wang, *Accurate and Simple Analytic Representation of the Electron-Gas Correlation-Energy*, Phys. Rev. B **45**, 13244 (1992).

[47] D. M. Ceperley and B. J. Alder, *Ground-State of the Electron-Gas by A Stochastic Method*, Phys. Rev. Lett. **45**, 566 (1980).

[48] M. Fuchs and M. Scheffler, *Ab initio Pseudopotentials for Electronic Structure Calculations of Poly-Atomic Systems Using Density-Functional Theory*, Comput. Phys. Commun. **119**, 67 (1999).

[49] M. Akdoğan and R. Eryiğit, *First-Principles Calculations on Vibrational and Dielectric Properties of Chalcopyrite $CuGaS_2$*, J. Phys: Cond. Matter **14**, 7493 (2002).

[50] R. Eryiğit, C. Parlak, and R. Eryiğit, *Ab initio Vibrational and Dielectric Properties of Chalcopyrite $CuInS_2$*, Eur. Phys. J. B **33**, 251 (2003).

[51] X. Gonze, *First-Principles Responses of Solids to Atomic Displacements and Homogeneous Electric Fields: Implementation of A Conjugate-Gradient Algorithm*, Phys. Rev. B **55**, 10337 (1997).

[52] C. Parlak and R. Eryiğit, *Ab initio Pressure-Dependent Vibrational and Dielectric Properties of Chalcopyrite $CuAlS_2$*, Phys. Rev. B **70**, 075210 (2004).

[53] H. W. Spiess, U. Heaberln, G. Brandt, A. Räuber, and J. Schneider, *Nuclear Magnetic-Resonance in I−III−VI$_2$ Semiconductors*, phys. stat. sol. (b) **62**, 183 (1974).

[54] T. Martin, J. M. Merino, J. L. Martin de Vidales, M. Leon, F. Rueda, and R. Diaz, *Stoichiometric Deviations Along An Ingot of CuGaSe$_2$*, Adv. Mater. Opt. Electron. **8**, 147 (1998).

[55] J. Krustok, J. Raudoja, J.-H. Schön, M. Yakushev, and H. Collan, *The Role of Deep Donor-Deep Acceptor Complexes in CIS-Related Compounds*, Thin Solid Films **361-362**, 406 (2000).

[56] P. Vinet, J. H. Rose, J. Ferrante, and J. R. Smith, *Universal Features of the Equation of State of Solids*, J. Phys: Cond. Matter **1**, 1941 (1989).

[57] L. Roa, J. C. Chervin, J. P. Etié, A. Polian, M. Gauthier, and A. Chevy, *High-Pressure Structural Study of CuAlS$_2$ and CuAlSe$_2$*, phys. stat. sol. (b) **211**, 455 (1999).

[58] R. S. Kumar, A. Sekar, N. V. Jaya, S. Nataraja, and S. Chichibu, *Structural Studies of CuAlSe$_2$, and CuAlS$_2$ Chalcopyrites at High Pressures*, J. of Alloys and Comp. **312**, 4 (2000).

[59] R. R. Reddy, Y. Nazeer Ahammed, K. Rama Gopal, P. Abdul Azeem, T .V. R. Rao, and P. Mallikarjuna Reddy, *Optical Electronegativity, Bulk Modulus and Electronic Polarizability of Materials*, Optical Materials **14**, 355 (2000).

[60] Q. B. Meng, C. Y. Xiao, Z. J. Wu, Ke-an Feng, Z. D. Lin, and S. Y. Zhang, *Bulk Modulus of Ternary Chalcopyrite A(I)B(III)C(2)(VI) and A(II)B(IV)C(2)(V) semiconductors*, Sol. Stat. Commun. **107**, 369 (1998).

[61] R. Asokamani, R. M. Amirthakumari, R. Rita, and C. Ravi, *Electronic Structure Calculations and Physical Properties of ABX(2)(A = Cu, Ag; B=Ga, In; X = S, Se, Te) Ternary Chalcopyrite Systems*, phys. stat. sol. (b) **213**, 349 (1999).

[62] M. Belhadj, A. Tadjer, B. Abbar, Z. Bousahla, B. Bouhafs, and H. Aourag, *Structural, Electronic and Optical Calculations of Cu(In,Ga)Se-2 Ternary Chalcopyrites*, phys. stat. sol. (b) **241**, 2516 (2004).

[63] B. H. Lee, *Elastic Constants of ZnTe and ZnSe Between 77 Degress-300 Degrees K*, J. Appl. Phys. **41**, 2984 (1970).

[64] A. Werner, H. D. Hochheimer, and A. Jayaraman, *Pressure-Induced Phase-Transformations in the Chalcopyrite-Structure Compounds - CuGaS$_2$ and AgGaS$_2$*, Phys. Rev. B **23**, 3836 (1981).

[65] A. Kraft, G. Kühn, and K. W. Möller, *Untersuchung von $CuGaSe_2$ und $CuGaTe_2$ unter Hohem Druck*, Zeitschrift für anorganische und allgemeine Chemie **504**, 155 (1983).

[66] O. H. Nielsen and R. M. Martin, *1st-Principles Calculation of Stress*, Phys. Rev. Lett. **50**, 697 (1983).

[67] D. R. Hamann, X. Wu, K. M. Rabe, and D. Vanderbilt, *Metric Tensor Formulation of Strain in Density-Functional Perturbation Theory*, Phys. Rev. B **71**, 035117 (2005).

[68] R. Fouret, B. Hennion, J. Gonzalez, and S. M. Wasim, *Elastic Stiffness Constants of Copper Indium Diselenide Determined by Neutron-Scattering*, Phys. Rev. B **47**, 8269 (1993).

[69] J. Lazewski, H. Neumann, P. T. Jochym, and K. Parlinski, *Ab initio Elasticity of Chalcopyrites*, J. Appl. Phys. **93**, 3789 (2003).

[70] M. Born and K. Huang, *Dynamical Theory of Crystal Lattices*, Clarendon Press, Oxford (1954).

[71] A. Filippetti and N. A. Spaldin, *Strong-Correlation Effects in Born Effective Charges*, Phys. Rev. B **68**, 045111 (2003).

[72] A. Debernardi, C. Ulrich, M. Cardona, and K. Syassen, *Pressure Dependence of Raman Linewidth in Semiconductors*, phys. stat. sol. (b) **223**, 213 (2001).

[73] R. Márquez and C. Rincón, *On the Dielectric-Constants of A(I)B(III)C(2)(VI) Chalcopyrite Semiconductor Compounds*, phys. stat. sol. (b) **191**, 115 (1995).

[74] X. Gonze, Ph. Ghosez, and R. W. Godby, *Density-Polarization Functional Theory of the Response of A Periodic Insulating Solid to An Electric-Field*, Phys. Rev. Lett. **74**, 4035 (1995).

[75] R. M. Martin and G. Ortiz, *Functional Theory of Extended Coulomb Systems*, Phys. Rev. B **56**, 1124 (1997).

[76] Ph. Ghosez, X. Gonze, and R. W. Godby, *Long-Wavelength Behavior of the Exchange-Correlation Kernel in the Kohn-Sham Theory of Periodic Systems*, Phys. Rev. B **56**, 12811 (1997).

[77] W. R. L. Lambrecht, E. Alldredge, and K. Kim, *Structure and Phonons of $ZnGeN_2$*, Phys. Rev. B **72**, 155202 (2005).

[78] D. N. Talwar and B. K. Agrawal, *Raman-Spectrum of Cubic Zinc-Sulfide - Interpretation*, phys. stat. sol. (b), **64**, 71 (1974).

[79] R. Trommer, H. Müller, M. Cardona, and P. Vogl, *Dependence of the Phonon-Spectrum of InP on Hydrostatic-Pressure*, Phys. Rev. B **21**, 4869 (1980).

[80] A. Debernardi and M. Cardona, *Isotopic Effects on the Lattice Constant in Compound Semiconductors by Perturbation Theory: An Ab initio Calculation*, Phys. Rev. B **54**, 11305 (1996).

[81] E. V. Iakovenko, M. Gauthier, and A. Polian, *Bond-Bending Modes and Stability of Tetrahedral Semiconductors under High Pressure: A Puzzle of AlN*, cond-matter/0301045 (2003).

[82] K. Kunc and R. M. Martin, *Density-Functional Calculation of Static and Dynamic Properties of GaAs*, Phys. Rev. B **24**, 2311 (1981).

[83] M. A. Subramanian, D. Li, B. A. Reisner, and A.W. Sleight, *High Dielectric Constant in ACu(3)Ti(4)O(12) and ACu(3)Ti(3)FeO(12) Phases*, J. Solid State Chem. **151**, 323 (2000).

[84] M. C. Ferrarelli, T. B. Adams, A. Feteira, D. C. Sinclair, and A. R. West, *High Intrinsic Permittivity in* $Na_{1/2}Bi_{1/2}Cu_3Ti_4O_{12}$, Appl. Phys. Lett. **89**, 212904 (2006).

[85] A. P. Ramirez, M. A. Subramanian, M. Gardel, G. Blumberg, D. Li, T. Vogt, and S. M. Shapiro, *Giant Dielectric Constant Response in A Copper-Titanate*, Solid State Commun. **115**, 217 (2000).

[86] Y. Liu, R. L. Withers, and X. Y. Wei, *Structurally Frustrated Relaxor Ferroelectric Behavior in* $CaCu_3Ti_4O_{12}$, Phys. Rev. B **72**, 134104 (2005).

[87] A. P. Ramirez, G. Lawes, V. Butko, M. A. Subramanian, and C. M. Varma, *Colossal Dielectric Constants in Braced Lattices with Defects*, cond-mat/0209498.

[88] Y. Zhu, J. C. Zheng, L. Wu, A. I. Frenkel, J. Hanson, P. Northrup, and W. Ku, *Nanoscale Disorder in* $CaCu_3Ti_4O_{12}$*: A New Route to the Enhanced Dielectric Response*, Phys. Rev. Lett. **99**, 037602 (2007).

[89] D. C. Sinclair, T. B. Adams, F. D. Morrison, and A. R.West, $CaCu_3Ti_4O_{12}$*: One-Step Internal Barrier Layer Capacitor*, Appl. Phys. Lett. **80**, 2153 (2002).

[90] M. H. Cohen, J. B. Neaton, Lixin He, and D. Vanderbilt, *Extrinsic Models for the Dielectric Response of* $CaCu_3Ti_4O_{12}$, cond-mat/0304196.

[91] P. Lunkenheimer, V. Bobnar, A. V. Pronin, A. I. Ritus, A. A. Volkov, and A. Loidl, *Origin of Apparent Colossal Dielectric Constants*, Phys. Rev. B **66**, 052105 (2002).

[92] P. Lunkenheimer, R. Fichtl, S. G. Ebbinghaus, and A. Loidl, *Nonintrinsic Origin of the Colossal Dielectric Constants in $CaCu_3Ti_4O_{12}$*, Phys. Rev. B **70**, 172102 (2004).

[93] L. He, J. B. Neaton, M. H. Cohen, D. Vanderbilt, and C. C. Homes, *First-Principles Study of the Structure and Lattice Dielectric Response of $CaCu_3Ti_4O_{12}$*, Phys. Rev. B **65**, 214112 (2002).

[94] L. He, J. B. Neaton, D. Vanderbilt, and M. H. Cohen, *Lattice Dielectric Response of $CdCu_3Ti_4O_{12}$ and $CaCu_3Ti_4O_{12}$ from First Principles*, Phys. Rev. B **67**, 012103 (2003).

[95] Guo-Ling Li, Zhen Yin, and Ming-Sheng Zhang, *First-Principles Study of the Electronic and Magnetic Structures of $CaCu_3Ti_4O_{12}$*, Phys. Lett. A **344**, 238 (2005).

[96] R. Weht and W. E. Pickett, *Magnetoelectronic Properties of A Ferrimagnetic Semiconductor: The Hybrid Cupromanganite $CaCu_3Mn_4O_{12}$*, Phys. Rev. B **65**, 014415 (2002).

[97] M. D. Johannes, W. E. Pickett, and R. Weht, *Structural Aspects of Magnetic Coupling in $CaCu_3Mn_4O_{12}$ and $CaCu_3Ti_4O_{12}$*, Mater. Res. Soc. Symp. Proc. **718** (2002).

[98] L. Chen and C. L. Wang, *First Principles Study of the Electron Structures of $CaCu_3Mn_4O_{12}$ and $CaCu_3Ti_4O_{12}$*, Journal of Magnetism and Magnetic Materials **312**, 266 (2007).

[99] R. K. Grubbs, E. L. Venturini, P. G. Clem, J. J. Richardson, B. A. Tuttle, and G. A. Samara, *Dielectric and Magnetic Properties of Fe- and Nb-doped $CaCu_3Ti_4O_{12}$*, Phys. Rev. B **72**, 104111 (2005).

[100] A. M. Rappe, K. M. Rabe, E. Kaxiras, and J. D. Joannopoulos, *Optimized Pseudopotentials*, Phys. Rev. B **41**, 1227 (1990).

[101] N. J. Ramer and A. M. Rappe, *Designed Nonlocal Pseudopotentials for Enhanced Transferability*, Phys. Rev. B **59**, 12471 (1999).

[102] Opium - Pseudopotential Generation Project, http://opium.sourceforge.net.

[103] X. Gonze and C. Lee, *Dynamical Matrices, Born Effective Charges, Dielectric Permittivity Tensors and Interatomic Force Constants from Density-Functional Perturbation Theory*, Phys. Rev. B **55**, 10355 (1997).

[104] D. Valim, A. G. Souza Filho, P. T. C. Freire, S. B. Fagan, A. P. Ayala, J. Mendes Filho, A. F. L. Almeida, P. B. A. Fechine, A. S. B. Sombra, J. Staun Olsen, and L. Gerward, *Raman Scattering and X-ray Diffraction Studies of Polycrystalline $CaCu_3Ti_4O_{12}$ under High-Pressure*, Phys. Rev. B **70**, 132103 (2004).

[105] Yanzhang Ma and Resul Aksoy, *Compression of $CdCu_3Ti_4O_{12}$ Perovskite to 55 GPa*, Solid State Commun. **142**, 376 (2007).

[106] S. B. Fagan, A. G. Souza Filho, A. P. Ayala, and J. Mendes Filho, *Ab initio Calculations of $CaCu_3Ti_4O_{12}$ under High Pressure: Structural and Electronic Properties*, Phs. Rev. B **72**, 014106 (2005).

[107] A. Koitzsch, G. Blumberg, A. Gozar, B. Dennis, A. P. Ramirez, S. Trebst, and S. Wakimoto, *Antiferromagnetism in $CaCu_3Ti_4O_{12}$ Studied by Magnetic Raman Spectroscopy*, Phys. Rev. B **65**, 052406 (2002).

[108] M. C. Mozzati, C. B. Azzoni, D. Capsoni, M. Bini, and V. Massarotti, *Electron Paramagnetic Resonance Investigation of Polycrystalline $CaCu_3Ti_4O_{12}$*, J. Phys.: Condens. Matter **15**, 7365 (2003).

[109] Naval Research Laboratory (NRL), Center for Computational Materials Science , http://cst-www.nrl.navy.mil

[110] Ph. Ghosez, J.-P. Michenaud, and X. Gonze, *Dynamical Atomic Charges: The Case of ABO(3) Compounds*, Phys. Rev. B **58**,6224 (1998).

[111] W. Zhong, R. D. King-Smith and D. Vanderbilt, *Giant LO-TO Splittings in Perovskite Ferroelectrics*, Phys. Rev. Lett. **72**, 3618 (1994).

[112] E. Kroumova, M. I. Aroyo, J. M. Perez Mato, A. Kirov, C. Capillas, S. Ivantchev, and H. Wondratschek, *Bilbao Crystallographic Server: Useful Databases and Tools for Phase-Transition Studies*, Phase Transitions **76**, 155 (2003).

[113] Thomas Riedle, *Raman Spectroscopy for the Analysis of Thin $CuInS_2$ Films*, Ph.D. thesis, Technischen Universitat Berlin (2002).

[114] E. Cockayne and B. P. Burton, *Phonons and Static Dielectric Constant in $CaTiO_3$ from First Principles*, Phys. Rev. B **62**, 3735 (2000).

CURRICULUM VITAE

Cihan Parlak

Address:

Abant İzzet Baysal University
Department of Physics,
Gölköy-Bolu, Turkey
Phone: +90 374 2541000
Fax: +90 374 2534642
Email: cihanparlak@gmail.com

Personal Details:

Gender: Male
Date of birth: 02nd of June, 1976
Place of birth: Bolu, Turkey

Education:

1995-1999 Undergraduate Studies in Physics at the Abant Izzet Baysal University

2000-2002 MSc in Physics at the Abant Izzet Baysal University
Thesis: Ab initio Calculations on Electronic and Lattice Dynamical Properties of Copper Indium Diselenide and Copper Indium Disulphide.

2002-2008 PhD in Physics at the Abant Izzet Baysal University
Thesis: First Principles Investigation of Lattice Dynamical Properties of Cu-Based Chalcopyrite Semiconductors and High Dielectric Constant Materials.

Specialization: Computational Condensed Matter Physics.

Publications:

1. Parlak C., Eryiğit R. "First principles electronic structure and lattice dynamics of giant dielectric compound $Na_{1/2}Bi_{1/2}Cu_3Ti_4O_{12}$" (in press).

2. Parlak C., Eryiğit R. "Ab initio volume-dependent elastic and lattice dynamical properties of chalcopyrite $CuGaSe_2$" Physical Review B 73, 245217 (2006).

3. Parlak C., Eryiğit R. "Ab initio pressure-dependent vibrational and dielectric properties of chalcopyrite $CuAlS_2$" Physical Review B 70, 075210 (2004).

4. Eryiğit R., Parlak C., Eryiğit R. "Ab initio vibrational and dielectric properties of chalcopyrite $CuInS_2$" European Physical Journal B 33, 251 (2003).

5. Parlak C., Eryiğit R. "Ab initio vibrational and dielectric properties of the chalcopyrite $CuInSe_2$" Physical Review B 66, 165201 (2002).

Presentations:

1. " First Principles Investigation of Electronical and Lattice Dynamical Properties of High Dielectric Constant Material $Na_{1/2}Bi_{1/2}Cu_3Ti_4O_{12}$" American Physical Society March Meeting, New Orleans-Louisiana (2008).

2. " First principles investigations into alkali intercalation of hexagonal boron nitride" American Physical Society March Meeting, New Orleans-Louisiana (2008).

3. "Electronic structure of chalcopyrite $CuInSe_2$: LDA and GW results" American Physical Society March Meeting, Denver-Colorado (2007).

4. "Ab-initio investigations on electronic and lattice dynamical properties on intercalation of Cu (copper) into hexagonal boron nitride(hBN). American Physical Society March Meeting, Denver-Colorado (2007).

5. "First principles investigation of Cu(Copper) intercalation in hexagonal boron nitride(hBN)" Turkish Chemical Society 20th Meeting, Kayseri-Turkey (2006)(Poster).

6. "Ab initio calculations on thermal properties of simple metals" Turkish Physical Society 22nd Meeting, Bodrum-Turkey (2004)(in Turkish).

Projects:

1. "Quantum mechanical investigation of structural electronic, optics and lattice dynamical properties of Ce and Ce-oxides and polarization properties of some high dielectric constant materials" AIBU Research Fund, Grant No. 04.03.02.199 (Researcher).

2. "Ab initio investigation of electronical, optical, lattice dynamical and polarization properties of some technologically important compounds." Tübitak, Grant No.TBAG-2449(104T057) (Researcher).

Working Experience:

1999-2008 Working in Abant Izzet Baysal University, Physics Department as an expert.